5-2013

Carrier Dynamics in InGaAs/GaAs Quantum Dots Excited by Femtosecond Laser Pulses

Kripa Nidhan Chauhan
Utah State University

Utah State University
MERRILL-CAZIER LIBRARY

CARRIER DYNAMICS IN InGaAs/GaAs QUANTUM DOTS

EXCITED BY FEMTOSECOND LASER PULSES

by

Kripa Nidhan Chauhan

A dissertation submitted in partial fulfillment
of the requirements for the degree

of

DOCTOR OF PHILOSOPHY

in

Physics

Approved:

_____   _____
D. Mark Riffe   Eric D. Held
Major Professor   Committee Member

_____   _____
David Peak   Shane Larson
Committee Member   Committee Member

_____   _____
Steve Bialkowaski   Mark R. McLellan
Committee Member   Vice President for Research and
                                                                      Dean of the School of Graduate Studies

UTAH STATE UNIVERSITY
Logan, Utah

2012

ABSTRACT

Carrier Dynamics in InGaAs/GaAs Quantum Dots

Excited by Femtosecond Laser Pulses

by

Kripa Nidhan Chauhan, Doctor of Philosophy

Utah State University, 2012

Major Professor: Dr. D. Mark Riffe

Department: Physics

Ultrafast carrier dynamics studies have been carried out on samples with single layers of self-assembled $In_{0.4}Ga_{0.6}As$/GaAs quantum dots (QDs). Measurements were made using femtosecond degenerate pump-probe differential reflectivity with an 800-nm, 28-fs Ti-sapphire oscillator as the source. The QDs were grown via modified Stranski-Krastanov growth. This modified growth process consists of two steps: low-temperature growth and high-temperature annealing. Specifically, the InGaAs QD structures are fabricated on *n*-type GaAs(001) using molecular beam epitaxy. The InGaAs layer is deposited at 350-370^{0}C followed by QD self assembly at 420-490^{0}C. Finally, these QDs are capped with 10 nm or 100 nm of GaAs. The measured width and height of these QDs are typically 25 nm and 8 nm, respectively. Dots annealed at higher temperature have larger base area (width and length) and reduced height, as compared to those annealed at lower temperature. We have used a model consisting of a linear combination of an exponential decaying function to describe the carrier dynamics and fit the reflectivity data, revealing trends in the carrier capture and relaxation times associated with the InGaAs layer versus laser excitation level and QD morphology. Capture times are ~ 1 ps for the 100-nm capped samples, but slightly shorter for the 10-nm capped thin samples, indicating carrier transport plays a

role in dynamics. The carrier dynamics in 10-nm capped samples are correlated with sample annealing temperature, indicating QD morphology affects carrier capture. Versus laser intensity, and thus carrier excitation level, the dynamics generally become slower, suggesting state filling is important in both the capture and relaxation of excited carriers in these samples.

(96 pages)

PUBLIC ABSTRACT

Carrier Dynamics in InGaAs/GaAs Quantum Dots

Excited by Femtosecond Laser Pulses

by

Kripa Nidhan Chauhan, Doctor of Philosophy

Utah State University, 2012

In semiconductors, everything is becoming smaller day by day; quantum dots are the smallest nanomaterials available today. Typical sizes of these quantum dots are in the range of 5 to 30 nm in diameter. Variations in size changes many material properties, such as electrical and nonlinear optical properties, making them very different from bulk semiconductors. The size of the QDs results in new quantum phenomena, which yield some extraordinary properties. Material properties change dramatically because quantum effects arise from the confinement of electrons and holes in the material. Hence, semiconductor quantum dots play an important role in designing new devices and technologies. To make new devices, the study of carriers (electrons and holes) in quantum dots plays a significant role.

Ultrafast spectroscopy has been used to study the carrier dynamics in quantum dots. Ultrafast spectroscopy was revolutionized in the 1980s by the invention of 100-fs (fs = 10^{-15}sec) pulses. In early 1990 a new revolution came in the field of lasers that produced ultra short pulses using Ti-sapphire oscillators. With these new Ti-sapphire lasers, one can produce laser pulses of 4-5 fs duration. These diode-pumped, solid-state lasers quickly replaced the expensive, large, and low-efficiency ion lasers. Ultrafast lasers can also be used to produce laser pulses with enormous peak power. In our lab, we produce 28-fs laser pulses with 1 nJ of energy. Each ultra-short pulse carriers power of 36 KW in our

lab. The ultra-short pulse allows one to create, detect, and study very fast relaxation in semiconductors. The use of ultra-short pulses has opened the door to many new findings in fundamental semiconductor mechanisms, especially those concerning carrier dynamics.

In this dissertation, we study carrier dynamics in quantum dots. Using the reflectivity experiment, we found capture times of electrons, i.e., how much time an electron takes to reach the quantum dot layer, and we have also measured relaxation times for carriers (when electron and hole relaxes) with the QDs.

Dedicated to my Mom and Dad,

my beloved wife, Mukta,

and our Children,

Prithika and Aarush

ACKNOWLEDGMENTS

I would like to express my sincere thanks and gratitude to Dr. D. Mark Riffe for his kindness and guidance that sailed me through my doctoral program. I am grateful for his time and patience to help me understand the subject better. It is his encouragement that kept me motivated and moving forward to achieve my goals. He has been a true inspiration for me for all these years. His guidance and patience motivated me to work in an exciting research setting and to grow as an independent experimentalist. I would also like to personally thank Dr. Eric Held for his unconditional support and encouragement, which came as a great help to me.

Further thanks go to all the members of my graduate advisory committee, namely, Dr. David Peak, Dr. Shane Larson, Dr. Eric Held, and Dr. Steve Bialkowski. This research would have not been possible without the quantum dot samples from Dr. Haeyeon Yang. I also thank F. K. Shen for taking AFM images of quantum dot samples. I would also like to thank James Coburn. It has been a great experience working with him in undergraduate labs. I would like to express my immense gratitude to Karalee Ransom for being extremely supportive and helping me throughout these years. For all administrative work, I want to thank Sharon Pappas for her help and assistance.

Many thanks also go to my friends for their moral support. I would like to thank Addison for the times he spent with me in figuring out the details of quantum dot samples. I would also like to express my thankfulness for John James, Nikhil Sharma, and Udit Dave. I also want to thank my fellow brilliant graduate friends in the Physics Department who helped me by switching my labs whenever I needed.

I am grateful to my mom and dad for their unconditional love, support, and all of the sacrifices they have made during my entire education. Most importantly, I would like to thank my wife, Mukta, who has been a great companion over this journey through the graduate school, which has been nothing but wonderful. She has always stood by my

side and inspired me to achieve my goals. Special thanks to my loving kids, Prithika and

Aarush, for helping me to keep things in perspective and reminding me to keep smiling.

CONTENTS

LIST OF TABLES

LIST OF FIGURES

CHAPTER 1

INTRODUCTION

One of the remarkable and dramatic developments in last five decades has been the application of solid-state physics to technical developments in electronic devices, such as transistors and semiconductor chips. The study of semiconductors led to the discovery of their important optical properties and numerous practical applications. In semiconductors, electronic transition from the valance band to the conduction band can easily be induced with the aid of a light. If the necessary energy is provided in the form of light, the wavelength at which that transition takes place can be found by observing a change in the absorption characteristics of the semiconductor. Reflectivity and ellipsometry, both of which are used in the experiment discussed in this dissertation, are two main techniques to characterize the optical properties of a semiconductor.

1.1   Optical Properties of Bulk and QDs

Because of their small size, quantum dots (QDs) display unique optical and electrical properties, as compared to bulk semiconductors. A key property of QDs is emission of photons under excitation. The photon emission wavelength depends not only on the material, but on the QD size. The ability to precisely control the size of a QD thus enables a manufacturer to tune the wavelength of emission over a wide range of wavelengths. The size dependence is derived from the basic physics principle that the quantized electronic energies depend sensitively upon the size of the constraining potential.

Semiconductor heterostructures containing self-assembled quantum dots are of fundamental interest because they provide a relatively simple means of producing an array of quantum potentials in which electrons and holes are confined in discrete quasiatomic (or zero-dimensional) energy states. In section 1, we discuss the physics behind the QDs, focusing on their optical properties. By varying the materials involved, the growth conditions,

and by vertically stacking layers of nanostructures, a rich variety of novel materials can be produced for the study of the fundamental properties of strongly confined systems, and for the development of advanced electronic and photonic devices. Any successful implementation of these quantum dots relies on their basic physical properties.

1.2 Why Study Quantum Dots?

Since the development in the growth of nanostructures, solid state physicists began to study QDs. Quantum dots provide an opportunity to investigate carrier dynamics in a finite size regime. Due to this confinement and resulting quantized energy structure, these materials have become the hub of many optical devices. We study quantum dots to understand the basic physics, including free-carrier capture and the relaxation of carriers within the dots. A main question, from the fundamental and technology point of view, is how do the semiconductor optical properties changes with size of QDs?

There is a big difference in the absorption spectrum of bulk and quantum dots: the bulk is spectrum continuous, while that of QDs is discrete in nature, as shown in Fig. 1.1. In semiconductors, the last filled band of allowed states is called the valence band (VB) and the next empty band is known as the conduction band (CB). Due to the broad spectrum, a wide range of transition energies exists from filled VB states to empty states of CB. This situation changes remarkably if the charge carriers are confined in three dimensions inside a small box. Since electrons exhibit both particle and wave properties, if the size of the box is small, the energy spectrum is quantized, i.e., discrete in nature.

A basic requirement for QDs is they should not be too small, otherwise they will have no localized states. QDs should not be too big, either. Otherwise the spacing between the energy levels becomes too small. Ideally, QDs should be uniform in shape and size and they should have a low density of defects. For InAs, QDs embedded in GaAs, it has been suggested the QD size should lie in the interval of 4 nm to 20 nm [1].
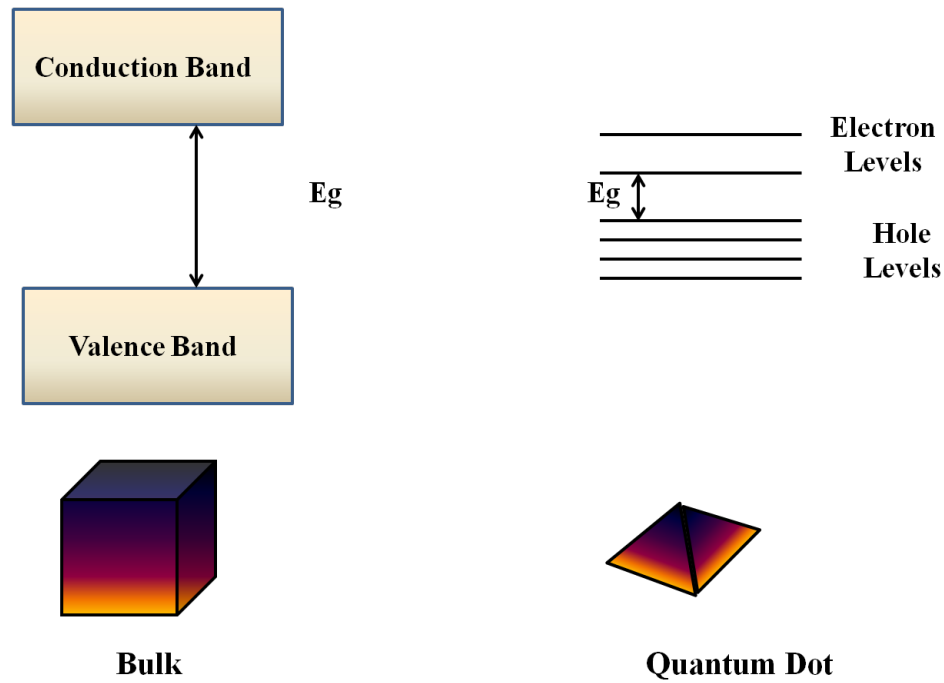
FIG. 1.1. Schematic representation of energy levels in a bulk semiconductor and a quantum dot.

1.3 Historical Development

The study of this quantum-size effect in thin layers of materials has been a fruitful area of research. Superlattices and their transport properties were first investigated by Esaki and Tsu [2, 3]. The 1970s was dedicated to semiconductor research on electronic structures with confinement limited to one dimension, known as quantum wells [4, 5]. The quantum well is very thin, flat layer of semiconductor sandwiched between two layers of another semiconductor, generally known as a heterostructure. The confinement of carriers (electrons or holes) becomes important when the thickness of the quantum well is comparable to the de-Broglie wavelength of the carriers. At present, the properties of quantum wells are well investigated and understood, and quantum-well devices have been produced and used for many years, in laser diodes in CD players, for example. In the 1980s rapid progress in fabrication technology, especially very accurate lithographic techniques, made

it possible to confine electrons in two dimensions, in structures known as quantum wires [6]. Complete quantization of an electron's free motion is implemented by trapping it in three dimensions, in structures known as quantum dots. This was first achieved by Reed and his group [7]. They reported the creation of square quantum dots with a side length of 250 nm, etched by the means of lithography. As a result of the three-dimensional confinement of electrons, quantum dot systems are similar to atoms. Fig. 1.2 illustrates this journey of semiconductor technology proceeding from the bulk to quantum dots. Unique discrete energy levels in QDs opened up a new area of fundamental research in semiconductors. In terms of fabrication, quantum-wire and quantum-dot structures constitute the utmost technological challenge.
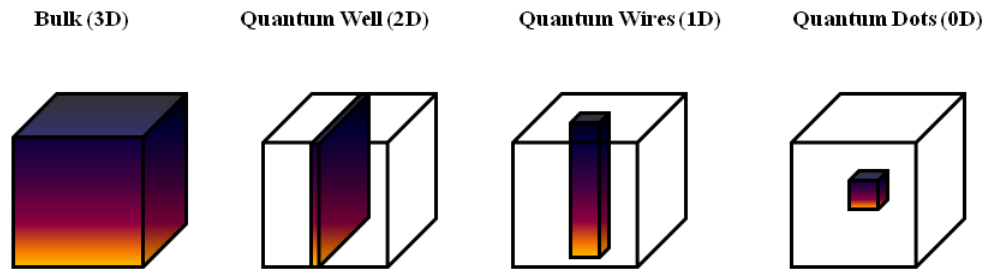
FIG. 1.2. Journey of semiconductor structures from bulk to QDs.

There are three main methods used to fabricate the QDs. The first method utilizes lithography. In this process quantum wells are patterned into dots. It was initially considered to be the easiest way to fabricate the QDs. But this process has several disadvantages, including contamination, low density, and defect formation. The second method is via colloidal synthesis. In this procedure QDs are formed through injection of reactants into a solvent solution. To form the crystalline structure of quantum dots the solvent is heated to a very high temperature and reactants are injected at very specific rates with very specific

timing. Typically II-V group QDs have been grown using this process. The third method is the self assembly of QDs. In the beginning of the 1990s, the discovery of self organization phenomena marked a breakthrough in the area of quantum dot growth. Self assembly is evolution of a two dimensional (2D) quantum well structure into an array of zero dimensional QDs. Self assembly can be achieved in conjunction with advance growth techniques like organic chemical vapor deposition (MOCVD) and molecular beam epitaxy (MBE). Stranski and Krastanov first proposed the possibility of spontaneous island formation initially on flat epitaxial surface [8]. Self assembled quantum dots have attracted attention as candidates for LEDs, solar cell devices and infrared detectors for example.

1.4 SK Growth of Quantum Dots

Molecular beam epitaxy (MBE) is a technique in which materials are grown layer by layer on the same crystalline lattice as a substrate. During the epitaxial growth process material is deposited under ultrahigh vacuum conditions at suitable deposition rates and substrate temperature. Epitaxy may be preserved even if the chemical composition is changed, but at the expense of some strain in the layer being grown. For example, addition of some In to the Ga beam in growing GaAs on GaAs substrate can lead to a perfect (but slightly strained) crystalline layer of InGaAs.

Islands will form when the decrease in strain energy exceeds the increase in surface energy. During the SK growth process, deposited material initially forms a thin 2D layer, which is know as the wetting layer (WL), on the top of which zero dimensional islands (the QDs) start to form as the layer exceeds a critical thickness. In general, the formation of islands leads to a reduction of the strain energy and an increase of the surface energy as compared to the planar case.

This transition from epitaxial 2D growth to island formation is quite abrupt when the layer thickness reaches the critical thickness. Defect-free islands are formed as a result of

the transition, and these islands are the quantum dots. This SK growth mode is traditionally used for growing QDs in III-V materials, such as InGaAs QDs on a GaAs substrate, as illustrated in Fig. 1.3. The shape and average size of the islands depend on the strain between the layer and substrate, the temperature at which growth occurs, and the growth rate. Figure 1.4 shows the dependence of the critical thickness of $In_xGa_{1-x}As$ monolayers deposited on GaAs substrate, as a function of the indium concentration [9, 10].
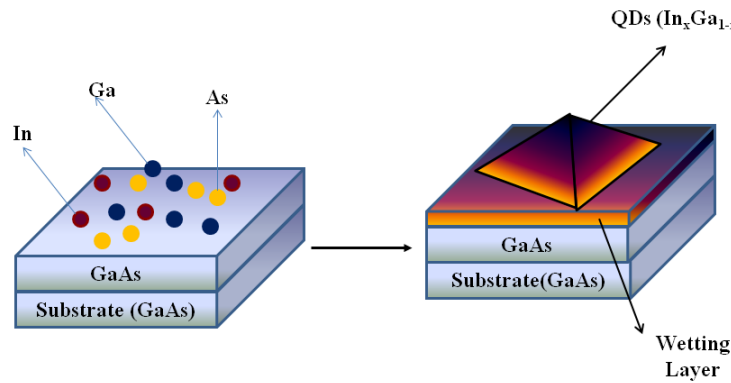
FIG. 1.3. Self assembly of Stranski-Krastanow growth mode.

Two issues with traditional SK growth are (i) random shapes of QDs and (ii) QDs positioning due to the surface segregation and intermixing between the substrate and epilayer. During growth, atoms tend to sit on the top of the substrate at sites with dislocations, grain boundaries, or stacking faults. This produces a nonuniform strain during the QD growth. Strain in epilayer greatly influences the shape of self-assembled QDs. In intermixing, molecules diffuse into the substrate and also in epilayer; this also plays an important role to control the size and shape QDs. Joyce and coworkers showed that intermixing is a temperature-dependent process, and it can be suppressed at the growth temperature of
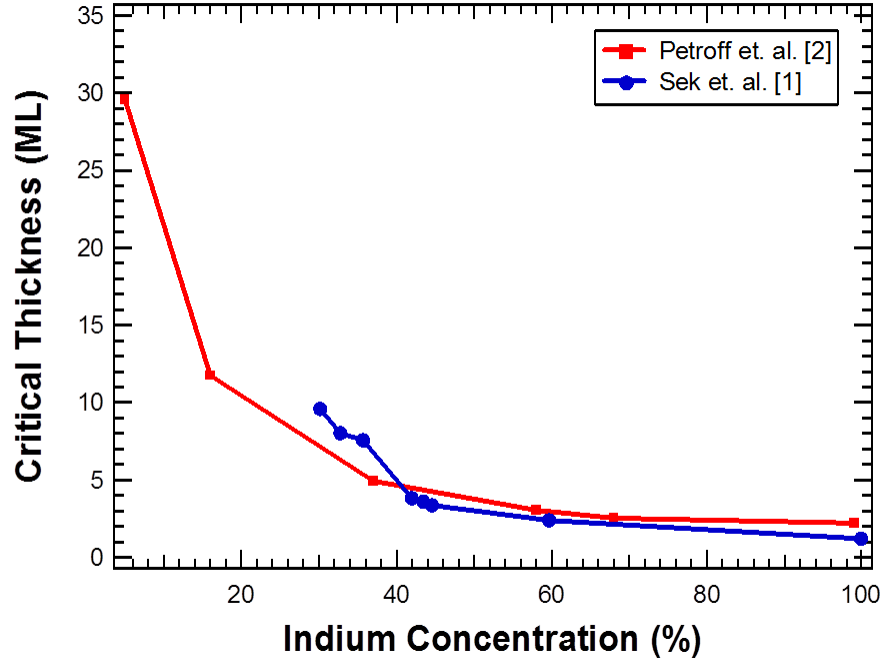
FIG. 1.4. Graph shows the In$_x$Ga$_{1-x}$As critical thickness as a function of In fraction x [9, 10].

420°C or lower [11]. Based on that observation, Yang and coworkers developed a new technique to grow QDs. In this technique an epitaxial InGaAs layer is grown at a sufficiently low temperature that layer-by-layer epitaxy can be achieved beyond the equilibrium critical thickness. The QDs are formed by annealing the sample to higher temperature. Yang and coworkers have shown the QD morphology depends upon InGaAs layer thickness and annealing temperature [12, 13].

1.5 Layout of Dissertation

In this dissertation, we have studied the dynamics of carriers interacting with the QDs in samples grown by Yang and coworkers. In Chapter 2, we will discuss the related work of carrier dynamics done on the InAs, InGaAs QD systems using time-resolved reflectivity, transmission, and photoluminescence. Chapter 3 will describe the experimental setup, theory, and basic formulas, which are required for the ellipsometry setup. In Chapter 4, we

will present the data collected on InGaAs/GaAs QD samples using pump-probe reflectivity.

Chapter 5 will describe the time-resolved ellipsometry setup.

CHAPTER 2

ULTRAFAST SPECTROSCOPY OF QUANTUM DOTS

2.1   Ultrafast Spectroscopy of Semiconductors

Since the 1960s optical spectroscopy has provided invaluable information on many diverse aspects of semiconductors, such as electronic band structure, phonons, excitation spectra of electrons and holes, and the properties of defects, surfaces, and interfaces. Popular techniques include absorption, reflection, luminescence, and light-scattering (Raman) spectroscopy. With the use of femtosecond (1 fs = 10^{-15} sec) and picosecond (1 ps = 10^{-12} sec) pulsed lasers, spectroscopy has become a prominent way to investigate these properties. The use of ultrashort pulses has opened the door to many new findings in fundamental semiconductor mechanisms, especially those concerning carrier dynamics. Since the development of the ultrafast laser, in particular the Ti-sapphire self-mode locking laser, ultrafast carrier dynamics have been studied in a great number of semiconductor systems. To observe such dynamics, it is important pulses have a shorter timescale than the timescale of the dynamics. Ultrafast spectroscopy of semiconductors has led to many new developments in the area of semiconductors and in many optoelectronic and electronic devices [14].

Thermal equilibrium is disturbed when an ultrafast laser pulse excites a semiconductor. The laser pulse initially creates a carrier distribution that can be characterized as having (i) a degree of (quantum) coherence [15, 16], (ii) both anisotropic and isotropic momentum-space components [17, 18], and (iii) a nonthermal energy distribution [19, 20, 21, 22]. Carrier-carrier scattering and carrier-phonon scattering relaxes these components in several, approximately sequential, ways. (i) On a timescale of a few tens of femtoseconds, the coherence disappears and the anisotropic components relax, resulting in an isotropic, incoherent distribution in momentum space [15, 16, 18]. (ii) On a timescale of 100 to 200 fs, the nonthermal energy distribution becomes thermalized, but is still hot [19, 20, 23]. (iii) This distribution then cools close to the initial sample temperature on a timescale of a few

ps [24]. (iv) On a much longer timescale the excited carriers eventually recombine across the energy gap, reestablishing a fully equilibrated state. In a sample with QDs, the excited carriers can be captured by the QDs and wetting layer, facilitating the eventual recombination process. From a technological point of view, this is important because these trapped carriers can participate in optical transitions associated with light detection or lasing, for example.

Several ultrafast laser techniques are widely used to investigate carrier dynamics in semiconductors. Pump probe spectroscopy is the most commonly used technique. In this technique, the laser pulses are divided into two parts, pump and probe. The sample under investigation is first excited by pump pulses and subsequently interrogated using the probe pulses, which are delayed in time with respect to the pump pulses. This technique divides into two common techniques: the probe beam is either transmitted or reflected from the sample under investigation. Time resolved THz spectroscopy also uses ultrafast femtosecond lasers and it works in a fashion similar to pump-probe spectroscopy. In a typical setup, the optical beam splits into two parts, the pump and the probe. The pump beam hits a terahertz photoconductive emitter and it emits a radiation in THz region. The THz radiation is transmitted through the sample. The probe beam gates the detector, whose response is proportional to the amplitude and the sign of the electric field of the THz-pulse. By changing the optical path between the pump and probe beam, information about the amplitude and phase of THz signals is obtained. Photoluminescence (PL) spectroscopy is a technique in which emission of radiation is induced by the optical excitation of the sample. Conventional PL spectroscopy is based on the measurement of the emission spectrum at fixed wavelength of exciting radiation. In time-resolved emission, the signal is measured as a function of the time delay after the excitation laser pulse.

2.2   Carrier Transport, Capture, and Relaxation

In the experiments presented in this dissertation, a photon with energy greater than the band gap of the material predominately excites carriers (electron-hole pairs) in the barrier (i.e., GaAs) on the either side of the InGaAs QD/wetting layer. Equilibration involving the InGaAs layer is schematically shown in Fig. 2.1 and can be described as follows:

1. Excitation of electrons from the barrier valence band into conduction band, creating free electron-hole pairs.

2. Transport to the region of InGaAs layer.

3. Carrier capture from the barrier to the wetting layer and excited states of the QD.

4. Carrier relaxation within the quantum layer via carrier-carrier scattering and carrier-phonon scattering.

5. Possible carrier transfer from the quantum dot to nearby deep levels, leading to carrier trapping and nonradiative recombination. This is only important if there are nearby deep levels.

6. Radiative recombination, in which electron and hole annihilate each other and release a photon. This is the ideal recombination process in a QD system.

This whole process of equilibration consists of four major processes: (i) transport of carriers to the InGaAs quantum layer, (ii) capture of carrier by quantum layer, (iii) relaxation within the quantum layer, and (iv) either radiative or nonradiative recombination. We now discuss the details of each of these first three processes, by which the carriers arrive in the ground state of QDs. As radiative recombination is typically in the range of nanoseconds, we do not consider the fourth process.
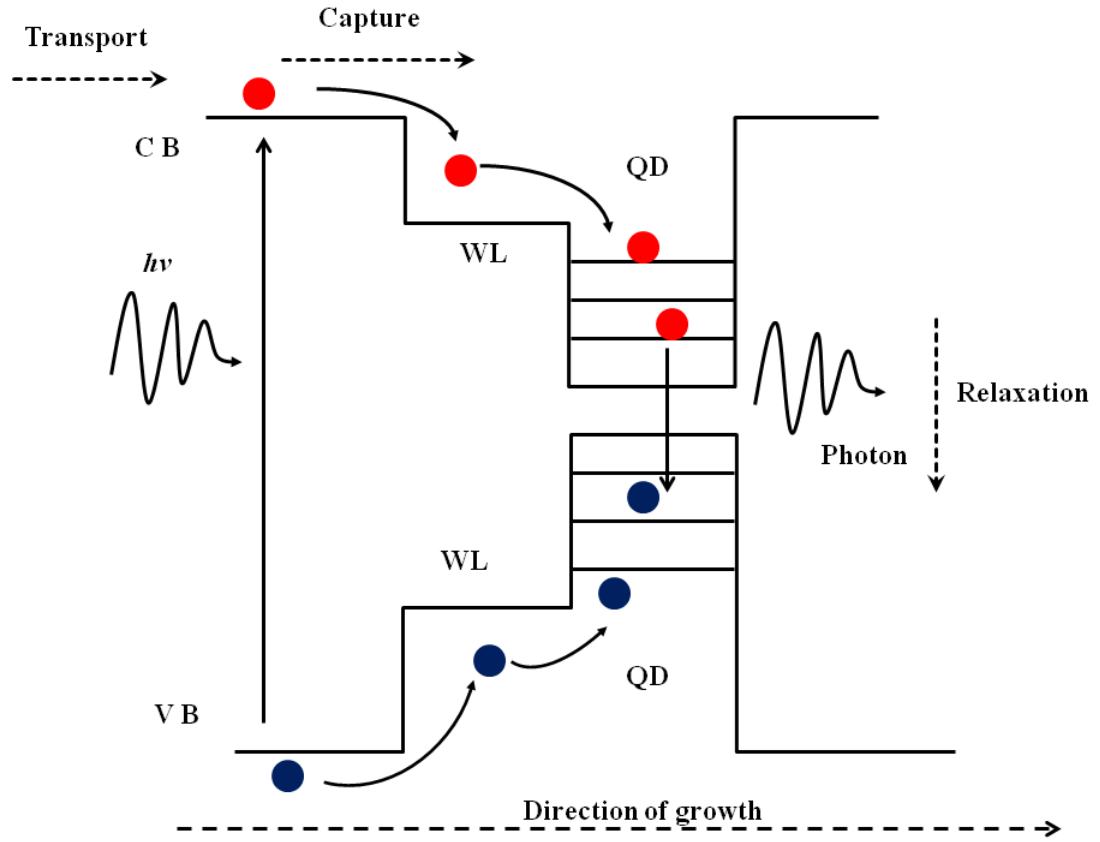
FIG. 2.1. Schematic of carrier dynamics involving wetting layer and quantum dots.

2.2.1 Transport of Carriers to the Quantum Layer

When a photon of an energy higher than the band gap of the semiconductor excites the carriers in the barrier, the majority of carriers are typically excited within approximately one micrometer from the surface. Considering the fact quantum dots (QDs) are usually near the surface of the sample, typically ≤100 nm from the surface, many carriers must travel a significant distance before being captured by the QDs. A number of studies have considered the transport of excited carriers to the region of the quantum layer. Using time-resolved photoluminescence (TRPL), Siegert and coworkers showed the transport time of carriers, when excited in the barrier, is ∼ 2 ps, independent of doping, and is much shorter than the ambipolar diffusion time, which is ∼ 130 ps at lower temperatures [25]. Marcinkevicius

and Leon studied how transport of carriers plays an important role determining the PL rise time [26]. Their QD samples were grown by depositing a 4.5 ML of $In_{0.4}Ga_{0.6}As$ and later these were covered by 100 nm of capping layer. The average diameter and areal density of QDs were 43 nm and 1×10^{10} cm^2, respectively. For comparison, quantum wells of the same composition and capping layer were also grown. Their PL studies indicated the room-temperature rise time for QWs is 1-2 ps, but for the QDs is 8 ps. Given these results, they conclude transport is not an important factor in determining the rise time. Sun and coworkers measured time resolved photoluminescence from QD samples capped with 50 nm of GaAs [27]. From analysis of PL rise times, they deduced the presence of a 12-ps component, which is close to the 10-ps diffusion time expected in their samples. These three examples illustrate assessing transport using TRPL is not straightforward, but, in general, it should be considered when carriers are excited in the barrier.

2.2.2 Carrier Capture by the Quantum Layer

Carrier capture refers to the process of carrier transfer from the continuum states of the barrier (GaAs) into the quantum-well-like wetting layer (WL) states or into the discrete QD states. Two scattering mechanisms are important for carrier capture, illustrated in Fig. 2.2. (i) The first process is carrier-carrier (Auger) scattering in which an electron or hole is captured from the barrier directly by transferring its energy to a second barrier electron or hole next to the QD. (ii) The second is capture with the emission of longitudinal-optical (LO) and/or acoustic phonons. Depending upon circumstances, either or both processes can be important to WL or QD capture. For example, as the excited carrier density is increased, Auger scattering becomes more important.

Uskov and coworkers have studied Auger capture dynamics using rate equations in InAs/GaAs quantum dot structures, calculating Auger capture coefficients for self-assembled quantum dots [28]. They show Auger capture times can be of the order of $1 - 100$ ps, de-

pending on barrier carrier densities and dot densities. Auger capture rates depend strongly on dot diameters and are greatest at dot diameters of about $10-20$ nm.
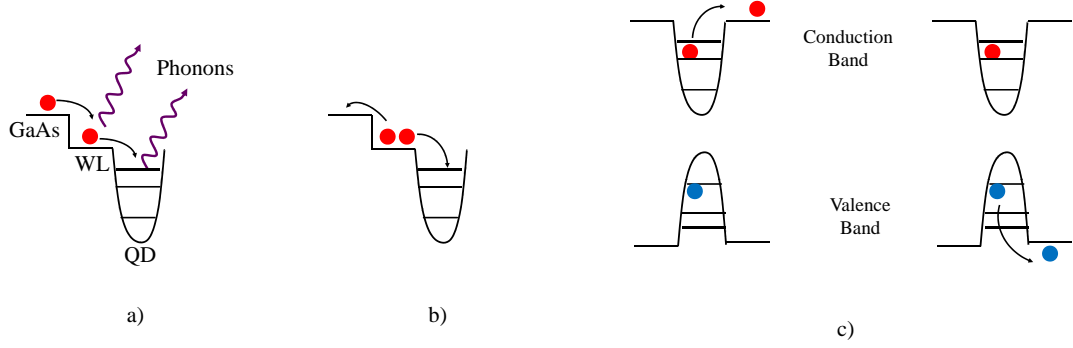
FIG. 2.2. Capture process in QDs. a) Multiphonon process. b) Auger scattering I. c) Auger scattering II.

Calculations of phonon-assisted capture of carriers in quantum dots, specifically, InAs QD systems have been reported by R. Ferreira and Bastard [29]. They pointed out LO-phonon-assisted capture presents strong resonances versus the dot size. Phonon assisted capture rates have been theoretically studied by Zhang and Galbraith [30]. Room temperature capture rates, capture with one or two LO, as well as LO and acoustic phonon participation, has been considered, and capture times of $3-5.5$ ps are obtained in densely populated InAs/GaAs quantum dots. Magnusdottir and coworkers calculate the capture time using Fermi's golden rule [31]. Temperature dependence of single-phonon capture times have been reported for the QDs density 5×10^{17} cm^{-3}, and it tends to decrease as the temperature increases. At high-carrier densities, the capture time tends to saturate because of the Fermi filling effect.

Carrier capture has also been studied experimentally. Sosnowski and coworkers measured an electron capture time of 2.8 ps from the barrier to the n=2 quantum dot state [32].

Liu studied carrier capture in InAs/GaAs QDs using pump-probe reflectivity [33]. In un-doped, as well as p-type samples, transfer times from the GaAs barrier to InAs WL is found to be between 0.2 and 1 ps, increasing with increasing excited carrier density, likely due to carrier saturation of QD levels. In studies by Li et al., carrier capture in InAs/GaAs hetero-structures were measured using pump-probe reflectivity [34]. They showed the capture time from the GaAs barrier to the InAs QDs strongly depends on the InAs layer thickness. Capture times from 0.5 to 17 ps were obtained. Muller et al. showed a capture time of ≤ 1 ps at room temperature using a pump-probe experiment on InAs/GaAs QDs with a dot den-sity of 2×10^{20} cm^{-3} [35]. Urayama and coworkers measured capture times for electrons of 2.5 ps and 2.0 ps at 40 and 290 K at low carrier densities, respectively, in an experiment using differential transmission on In$_{0.4}$Ga$_{0.6}$As quantum dots, [36]. PL rise times between 2 and 4 ps have been measured and attributed to electron capture [27]. Zhang and cowork-ers used TRPL to measure a rise time of ~ 1 ps for n=1 QD state, which they interpret as due to carrier capture [37].

Lobo and coworkers have measured rise times of high density (2.5×10^{10} cm^{-2}) and low density (7×10^8 cm^{-2}) QDs [38]. As a function of temperature, the rise time decreases with the increase in temperature for low-density QDs from 15-5 ps, but for high-density QDs, it does not change much, from 6-4 ps. Marcinkevicius and coworkers also found the QD density has a significant influence on the carrier transfer to QDs [39]. For the low QD density structures, carrier transfer is inhibited by potential barriers at the barrier/quantum dot interfaces. They also found as the temperature and excitation intensities increase, the capture time decreases.

To summarize, carrier capture depends on a number of factors, including the density of QDs and excitation intensity. Typical capture time vary from several hundred fs to few ps. Capture times are governed by Auger scattering and phonon emission.

2.2.3 Carrier Relaxation within the Quantum Layer

As opposed to the bulk, where carriers can relax through a continuum of states, in a QD, only a small set of discrete states lies between the WL continuum and the QD ground state. Early on, this was expected to dramatically slow down relaxation due to suppression of LO-phonon emission, when the phonon energy does not equal the level spacing in the QDs. Therefore, much work has centered on the reality of this phonon bottleneck. A theme that has emerged is carrier-carrier scattering must be suppressed in order for the phonon bottleneck to be manifest.

Carrier relaxation has been explained by many mechanisms, including phonon bottleneck, carrier-carrier scattering, carrier-phonon scattering, and defect-assisted relaxation. Nielsen and coworkers carried out a detailed analysis of carrier-carrier scattering and carrier-LO phonon scattering [40]. Their calculations were not restricted to Fermi's golden rule, but also included population effects. Carrier screening of the QD-WL interaction was also considered. For higher densities, the carrier capture time was longer than the relaxation time: carrier-carrier relaxation time was 1 ps and the capture time was 10 ps. Fast relaxation times have been calculated by Uskov and coworkers in self-assembled QDs. If the carrier density in the surrounding barrier is sufficiently high, Auger relaxation times were found in the range of 1-10 ps for the carrier densities of 10^{11}-10^{12} cm^{-2} [41]. Ferreira and Bastard calculated the capture and relaxation of carriers in quantum dots, specifically, InAs/GaAs self-assembled dots. They pointed out Auger relaxation is extremely fast in these structures. They also found that relaxation times are around 1-10 ps due to carrier-carrier scattering [29]. Phonon bottleneck has been reexamined by Li and coworkers in an attempt to check this mechanism within the intrinsic phonon scattering [42]. Their calculation demonstrated the efficient carrier relaxation of 2.5-7 ps for QDs larger than 15 nm in size. The relaxation in quantum dots has been discussed using phonon scattering mechanism. Schroeter and coworkers calculated the relaxation of carriers in In$_{0.5}$Ga$_{0.5}$As QDs

with the average size of 10 nm at low temperature [43]. They found relaxation through defects may circumvent the phonon bottleneck predicted for ideal nanometer-scale quantum dot structures, even at low temperatures.

Continuum background is the process by which carriers relax quickly within the continuum states in barrier and wetting layers and then make transitions to the ground state by phonon scattering. This mechanism was first observed by Toda and coworkers [44]. According to their model, electrons first relax through the continuum with the emission of longitudinal acoustic (LA) phonon and then it relaxes to the QD ground state with the LO phonon emission. Theoretically, Vassanelli and coworkers showed it is this process by which carriers are indirectly transferred from barrier/WL to discrete QD states [45].

Toda and coworkers investigated relaxation processes in InGaAs QDs with diameter 20 nm, a height of 7 nm, and density of 10^{10} cm^{-2} [44]. They strongly suggested the existence of continuum states in single dots. The density of states gradually increases from the end of QD to the wetting layer absorption edge. For excitation of carrier at the WL absorption edge, the carriers can relax quickly through the continuum states by LA phonon scattering and transition to the excitonic ground state by strong electron-phonon interactions, which is attributed to intradot relaxation in QDs. Bogaart and coworker have measured the capture time at room temperature in InAs/GaAs quantum dots grown by chemical beam epitaxy. They measured photoluminescence (PL) spectrum, as well as differential reflectivity, using two-color, pump-probe reflectivity, where the pump excites carriers in the barrier and the probe is tuned to transition from ground state to excited state. Their continuum model is as follows: an electron first relaxes via continuum states in the barrier, emitting a single LO phonon and then is captured by QDs. They suggested the efficiency of this relaxation model directly depends on coupling strength between the continuum states and the discrete energy level in QDs. They studied the carrier capture and relaxation in self-assembled InAs/GaAs quantum dots (QDs) using bleaching rise-time measurements as a function of

the excitation density at 5, 77, and 293 K. They observed the bleaching rise time and the carrier lifetime of the first excited state are longer than the bleaching rise time of the QD ground state, indicating the excited state does not act as an intermediate state.

For high excitation density, Bogaart and coworkers observed a temperature-dependent plateau in the initial bleaching rise time, contradicting an Auger-scattering-based relaxation model [46]. For higher excitation densities, the Auger carrier relaxation through the continuum is very fast and is followed by a single LO-phonon emission toward the QD ground state. The time scale for this process is around 5-10 ps.

Phonon bottleneck has been verified by Urayama and coworkers where they excite only one electron-hole pair per dot at very-low excitation densities [47]. This phenomenon is observed at low carrier density and at low temperatures. They performed time resolved transmission experiment on InGaAs QDs at low carrier densities, in which nongeminate capture (one electron in one QD and hole in other QD) of carriers take place. In this regime they found a very long time scale of 750 ps for carriers to relax in the QDs. Work by Heitz and coworkers suggest a suppressed exciton relaxation for self-organized InGaAs/GaAs QDs. A low-temperature relaxation time of 7.7 ns leads to a pronounced phonon-bottleneck effect [48]. Ikeda and coworkers studied the phonon bottleneck effect in InAs/GaInP quantum dots (QDs) [49]. The time-resolved photoluminescence spectra in QDs are measured in the temperature range of 5-200 K. They found carrier relaxation at low temperature is about 500 ps.

There are several other interesting results concerning carrier relaxation. Gundogdu and his coworkers showed an ultrafast carrier capture and relaxation time on InAs QDs by time resolved PL. They found faster relaxation times for InAs QDs to be 4.8 ps and this faster relaxation times are attributed to carrier-carrier scattering [50]. Marcinkevicius and his coworkers grew InGaAs QDs at different annealing temperatures from 700 ^{0}C to 900 ^{0}C. Low-temperature annealing QDs are smaller in size than high temperature. Carrier transfer

in low-temperature annealing dots is faster. They observe a direct confirmation of efficient carrier relaxation in quantum dots by optical phonon emission. With the increase in carrier density, PL rise time tends to decrease, and this is due to carrier relaxation via auger process [51]. A capture time of 3 ps has been measured using differential transmission measurements by Wesseli [52].

CHAPTER 3

EXPERIMENTAL AND SAMPLE DETAILS

The aim of this dissertation is the study of carrier dynamics in semiconductor QDs after femtosecond pulse excitation. I have investigated the dynamics using two experiments: time-resolved differential reflectivity (TRDR) and time-resolved ellipsometry (TRE). The complex index of refraction ($N = n - ik$) is an important parameter for the characterization of the semiconductors QDs and for optoelectronic devices. Time-resolved reflectivity of a semiconductor typically provides information on the change in the real part of the index. For example, the change in n carrier dynamics in silicon have been studied in our lab using time-resolved reflectivity [53]. But in order to directly access the change in absorption we need to probe changes in the imaginary part of the index (k). Thus, we have worked to extend the measurements so we can study both changes in n and k. Ellipsometry is the tool that will give us the full information about the index of refraction (or equivalently the dielectric function) of the semiconductor, and thus, has the potential to give more insight into carrier dynamics as compared to simple pump and probe reflectivity [54].

3.1 Laser System and Diagnostics

A highly stable home-built Ti-sapphire laser based on the design of Asaki *et. al.* operating at 800-nm wavelength and producing 17-fs full-width-half-maximum pulses at a repetition rate of 88 MHz is used in my experiments [55]. The energy of each pulse is 1 nJ. As illustrated in Fig. 3.1, interferometric autocorrelation traces obtained with a rotating-mirror autocorrelator are used to determine the laser pulse width and confirm the near-Gaussian nature of the pulses [56].

3.2 Light Reflection at an Interface

The samples studied here consist of multilayer GaAs/InGaAs/GaAs structures; because of this, the reflectivity of the samples depends upon the optical properties of GaAs, InGaAs,
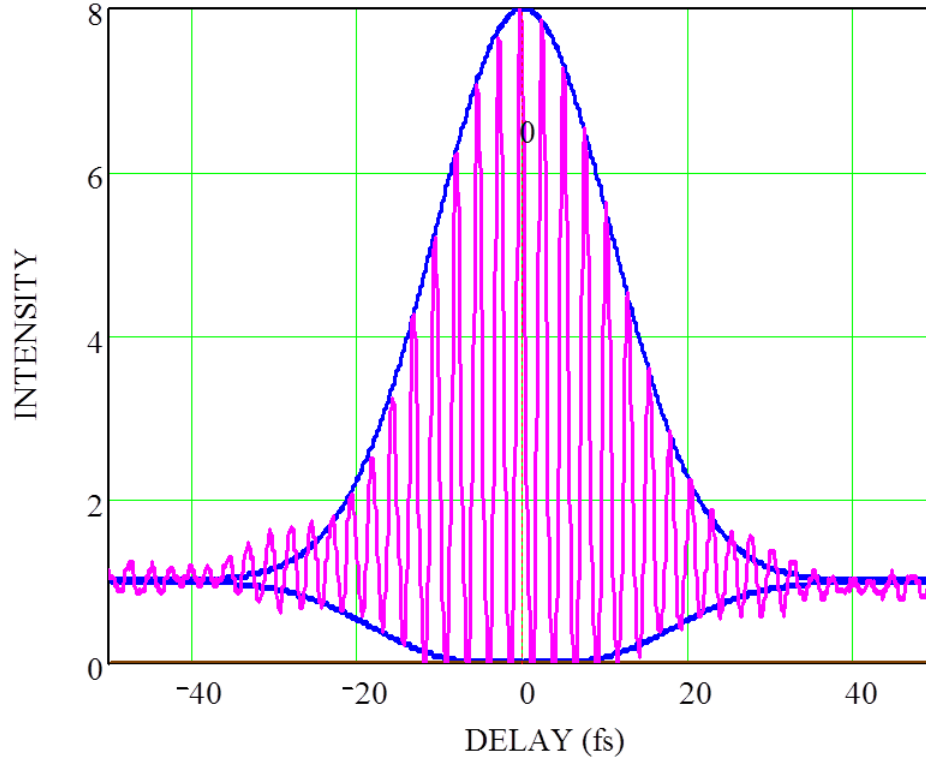
FIG. 3.1. Interferometric autocorrelation trace with a FWHM of 17.6-fs pulse consistent with Gaussian shape envelope function (top and lower) from Ti-sapphire laser with 106 mW of pump power.

and the exact near-surface structure of these two materials. However, in our experiments, we expect the dominant effect upon reflectivity to be due to the carriers that are excited within the GaAs cap and base. We thus simply consider the reflectivity that occurs at an air/GaAs interface, but at the same time we recognize changes in the InGaAs optical properties may also be important to our measurements.

As illustrated in Fig. 3.2, we consider plane-wave light traveling in a medium with index N_0 that is incident on another medium with index N_1. For this situation the reflection amplitudes r_p and r_s for p and s polarized light are respectively given by
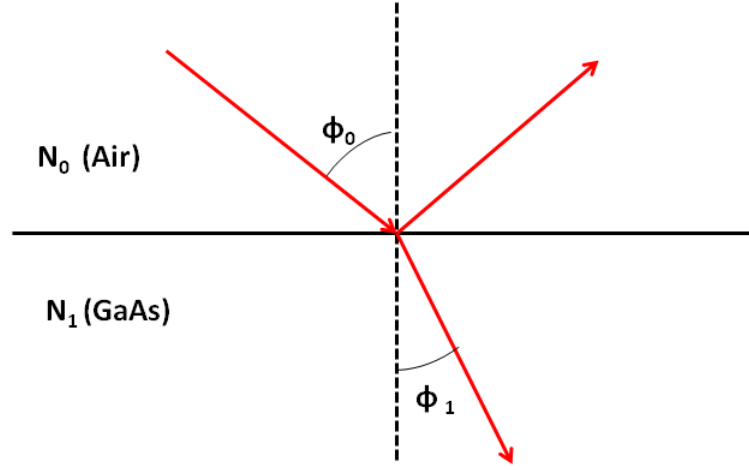
FIG. 3.2. Reflection and transmission at the interface between the two mediums.

$$r_p = \frac{E_{rp}}{E_{ip}} = \frac{N_1 \cos(\phi_0) - N_0 \cos(\phi_1)}{N_1 \cos(\phi_0) + N_0 \cos(\phi_1)}, \tag{3.1}$$

and

$$r_s = \frac{E_{rs}}{E_{is}} = \frac{N_0 \cos(\phi_0) - N_1 \cos(\phi_1)}{N_0 \cos(\phi_0) + N_1 \cos(\phi_1)}. \tag{3.2}$$

Here the Es are the complex electric field amplitudes and the subscripts r, i, p, and s refer to reflection, incident, p polarization, and s polarization, respectively. Although complex, the angle ϕ_1 is given by Snell's law,

$$\sin(\phi_1) = \frac{N_0}{N_1} \sin(\phi_0). \tag{3.3}$$

In order to separate the effect of reflection on the amplitude and phase of the wave, we rewrite the complex Fresnel amplitudes as

$$r_p = |r_p| e^{i\delta_p}, \tag{3.4}$$

and

$$r_s = |r_s|e^{i\delta_s}. \tag{3.5}$$

$|r_p|$ and $|r_s|$ give the ratio of the amplitudes of electric field vectors of the reflected wave to that of the incident wave, while δ_p and δ_s give the phase shifts upon reflection [57].

Reflection coefficients, which give the ratio of reflected to incident intensity, are the square modulus of the amplitudes. That is,

$$R_s = ||r_s|e^{i\delta_s}|^2, \tag{3.6}$$

and

$$R_p = ||r_p|e^{i\delta_p}|^2. \tag{3.7}$$

Changes in these coefficients are measured in our experiments.

3.3 Time Resolved Pump-Probe Differential Reflectivity

A pump-probe experiment utilizes two pulses. One pulse is known as the pump pulse, which induces the changes in the material. After a certain time delay, a second, typically weaker pulse, known as the probe, interrogates the area of the sample that was excited, and a photo-detector measures the signal from the probe. We vary the delay between the pump and a probe pulse by changing the distance the pump has to travel before reaching the sample. Thus, we can measure the reflectivity of the material for different time delays after the pump pulse, revealing the time-dependent material changes after the pump pulse has excited the sample.

In our lab, we have a pump-probe experimental set up, as illustrated in Fig. 3.3. Linearly polarized pulses from the Ti:sapphire laser pass through a half-wave plate (HWP),

which rotates the beam polarization to the desired angle and allows us to adjust the relative intensities of the pump and probe pulses. After the HWP, the pulses pass through a beam splitter, which splits each laser pulse into two orthogonally linearly polarized pulses, the pump and probe. The pump pulse (*p*-polarized) travels through a delay stage and then hits the sample at normal incidence. The probe pulse (*s*-polarized) is incident on the sample at 45 degrees. The reflected probe pulse then passes through the calcite polarizer, which is set for the maximum transmission of reflected probe light, and thus minimum transmission of scattered light, from the probe. The intensity of the reflected probe pulse is detected by a Si photodiode detector. The chopper modulates the pump beam in an approximately on-off fashion, modulating the excitation of the sample. The resulting modulated reflectivity of the probe is recorded using a lock-in amplifier. In terms of the pump-induced changes in *n* and *k* of the sample, change in probe reflectivity can be expressed as

$$\frac{\triangle R(t)}{R} = \frac{1}{R}\frac{\partial R}{\partial n}\triangle n(t) + \frac{1}{R}\frac{\partial R}{\partial k}\triangle k(t), \tag{3.8}$$

where $\triangle R = R(n,k) - R(n_0,k_0)$, and $\frac{1}{R}\frac{\partial R}{\partial n}$ and $\frac{1}{R}\frac{\partial R}{\partial k}$ are the *n*-differential and *k*-differential coefficients, respectively. $R(n_0,k_0)$ is the reflectivity when no pump beam is used. $\frac{\triangle R}{R}$ is the experimentally observed quantity. In a typical reflectivity experiment on a semiconductor $\frac{1}{R}\frac{\partial R}{\partial n} \gg \frac{1}{R}\frac{\partial R}{\partial k}$, that is, the differential reflectivity is typically much more sensitive to $\triangle n$ than $\triangle k$. Figure 3.4 plots differential coefficients for both *s*- and *p*-polarized waves. As shown, for *s*-polarization $\frac{1}{R}\frac{\partial R}{\partial n} \gg \frac{1}{R}\frac{\partial R}{\partial k}$ for all incident angles. For *p* polarization, the two differential coefficients can be comparable, but only near the Brewster's angle, as illustrated in Fig. 3.4 (b). Unfortunately, this is where *R* becomes quite small, and measurements are difficult in this region. Appropriate for our *s*-polarized probe beam, the change in reflectivity is given to good approximation by
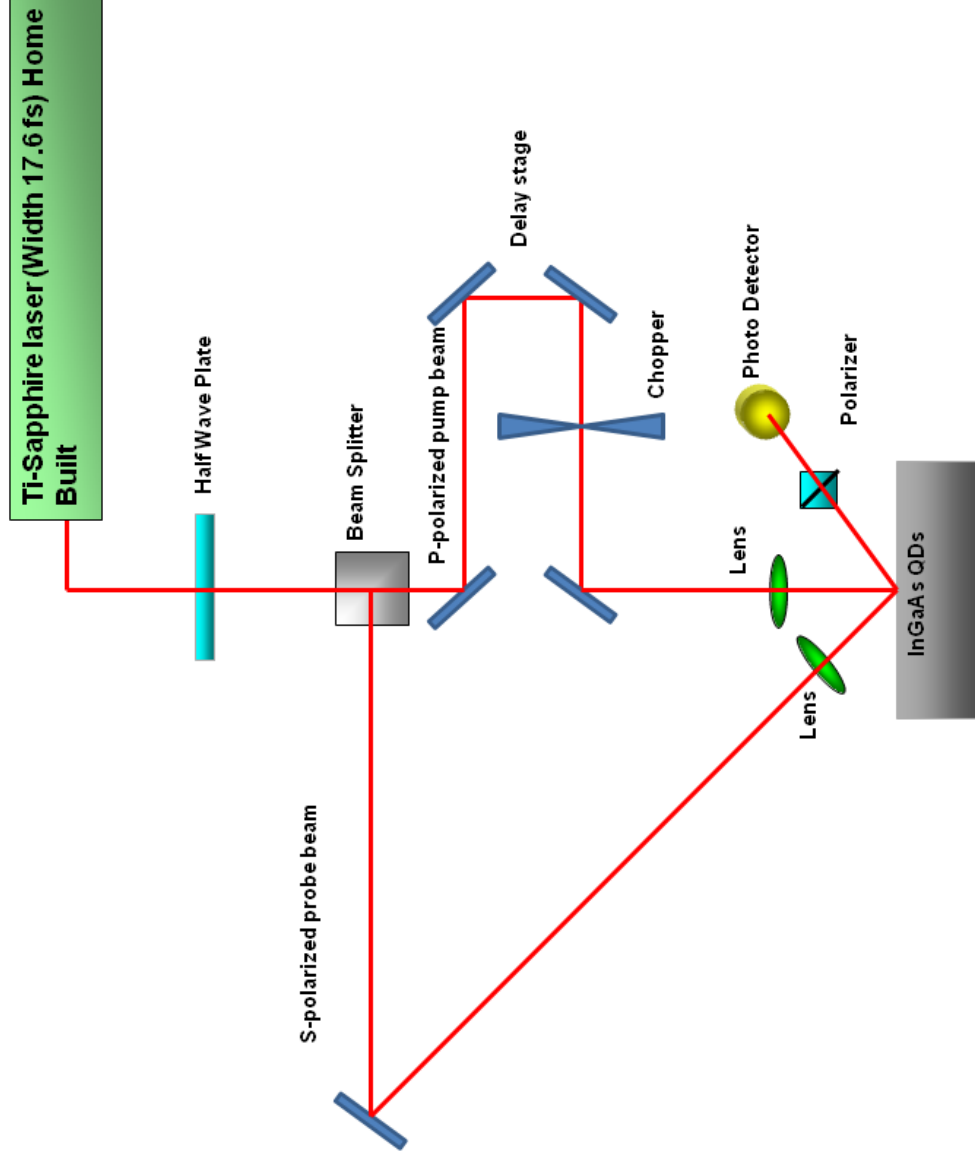
FIG. 3.3. Schematic diagram for time-resolved pump probe differential reflectivity (*TRDR*). The ultrashort laser pulse is split into pump and probe pulse with a delay stage. The pump pulse is used to excite the sample, whereas the probe pulse measures the changes induced by the pump.

$$\frac{\triangle R_s}{R_s} = \frac{4n_0 \cos(\theta)}{(n_0^2 - 1)[n_0^2 - \sin^2(\theta)]^{1/2}} \triangle n, \tag{3.9}$$

where θ is the angle of incidence [53].

3.4 QD Sample Details

As mentioned in Section 1, the QD samples studied here have been grown by Yang and coworkers using a new technique. Before discussing the growth and morphology of these samples, we briefly review traditional Stranski-Krastanov (SK) growth of InGaAs QDs on GaAs. Traditional SK growth of InGaAs QDs is divided into three steps: (i) oxide removal, (ii) GaAs buffer layer growth, and (iii) InGaAs growth and self assembly. First the oxide is desorbed from the surface by heating the GaAs substrate to 620^0C in ultra high vacuum. Subsequent to oxide desorption, a GaAs buffer layer is grown, typically for one hour at a growth temperature of 580°C. This provides an atomically flat surface for the InGaAs growth. The InGaAs QD layer is then grown, typically at a growth rate of ~ 0.1ML/sec at a temperature of 460^0C. In the SK growth mode, surface segregation of indium is a serious issue of the InGaAs quantum layer growth, since Indium atoms tend to move to the top layer of the InGaAs layers. To overcome this issue, Yang and coworkers modified the traditional SK growth.

3.4.1 Modified SK Quantum Layer Growth

In Yangs's modified SK growth method, step (iii) of the traditional SK growth is divided into two steps: low-temperature growth of flat InGaAs layer followed by a high-temperature anneal, during which QDs self assemble. The growth details of samples studied here are as follows. First, 800 to 1500 nm of GaAs buffer layer is grown at 575^0C to 595^0C for three hours. Then, 10 to 15 ML of flat InGaAs QD layer is grown at 350^0C to 370^0C. The post-growth annealing is then performed: the sample is heated to a temperature
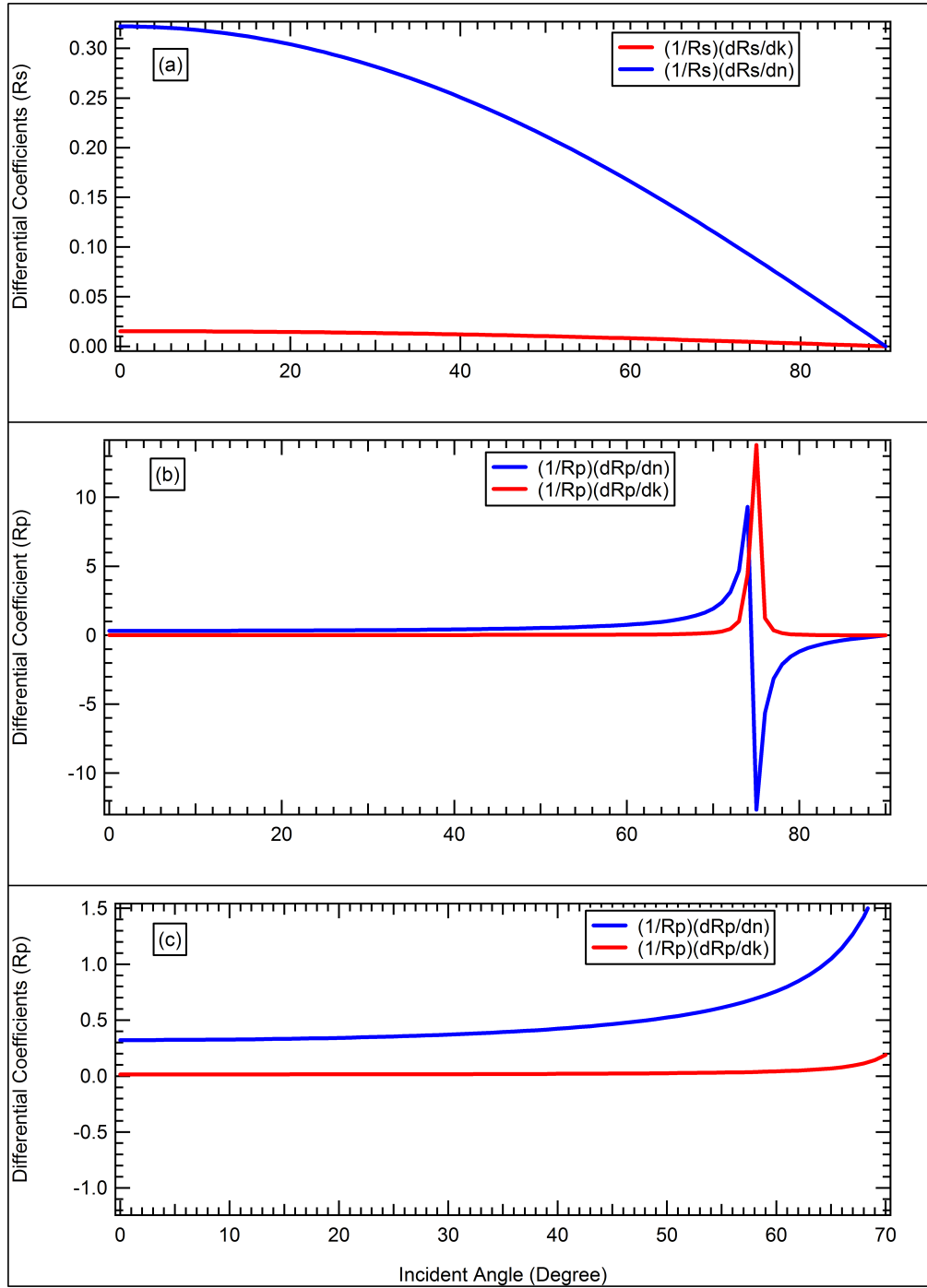
FIG. 3.4. Differential coefficients of reflectivity in TRDR experiment. (a) Differential coefficients of reflectivity R_s. $\frac{1}{R}\frac{\partial R}{\partial n}$ is larger than $\frac{1}{R}\frac{\partial R}{\partial k}$. (b) Differential coefficients of reflectivity R_p. (c) At 45^0 figure shows $\frac{1}{R}\frac{\partial R}{\partial n}$ is again larger than $\frac{1}{R}\frac{\partial R}{\partial k}$.

in the range of 420^0C to 490^0C for 120 seconds. Reflection high-energy electron diffraction (RHEED) is used to conform the formation of QDs. After this, a cap layer of either 10 or 100 nm of GaAs is deposited on InGaAs QD layer. 10-nm and 100-nm samples are referred here as thin cap and thick cap, respectively. Details of each sample can be found in Tables 3.1 and 3.2. Samples from A to E are thick-capped samples (100 nm) and F to J are thin-capped samples (10 nm).

3.4.2   AFM Images of QD Layer

To study the surface morphology of InGaAs QD, *ex situ* atomic force microscopy (AFM) measurements have been performed. These images show a prominent presence of QD structures even though they are capped with a layer of GaAs. AFM images from Fig 3.5 to Fig 3.9 are from the thick-cap samples. Images from samples B, D, and E show nearly identical patterns of QD patches. All of these three samples have a ~10 ML deposition of InGaAs at a growth temperature of 350^0C to 360^0C. Figure 3.10 to 3.14 show images of thin-cap QD samples. Samples F, G, and J have a 15 ML deposition of InGaAs, while samples I and H have a 10 ML deposition. AFM images of samples C and H do not show any formation of quantum dots, in agreement with the RHEED observations. In contrast to the RHEED measurements, sample H shows no indication of QD formation. AFM images of samples F, G and I shows a clear resemblance to the *in situ* scanning tunneling microscopy (STM) measurements of other uncapped QDs grown under similar conditions [12]. Those STM measurements show a typical QD base width of ~20 nm and height of ~8 nm.

TABLE 3.1. $In_{0.4}Ga_{0.6}As$ quantum dot sample details of thick GaAs cap.

		Thick Cap QD Samples				
	Sample	A	B	C	D	E
	Serial #	041007-1	041007-2	041707-1	041707-2	040607-1
Buffer	Moly/Plate	/a	/u	/u	/a	/a
	Growth Temp(°C)	585	595	595		
	Growth Rate(ML/s)	0.615	0.61	0.56	0.59	0.61
	Growth Time	1hr 23 min	1hr 56 min	1hr 36 min		1hr 44 min
	Thickness (nm)	866.7	1203.5	912.8		1082.5
QD Layer	Growth Temp(°C)	350	360	360	350	350
	As (%)	20	20	20	20	20
	Growth Rate(ML/s)	0.238	0.19	0.19	0.2	0.161
	Growth Time (sec)	50	50	50	50	47
	Thickness (ML)	11.924	9.47	9.49	10	7.3
	Thickness (nm)	3.19	2.68	2.68	2.83	2.15
Annealing	Temp (°C)	450	440	420	430	470
	Time (sec)	120	120	120	120	120
RHEED	Q Dot	Y	Y	N	Y	Y
Low-Temperature Cap	Substrate Temp (°C)	450	440	420	430	470
	As (%)	25	25	20	25	25
	Growth Rate(ML/s)	0.155	0.121		0.12	0.12
	Time (sec)	295	295	295	295	295
	Thickness (ML)	45.729	35.631		34	36.58
	Thickness (nm)	12.954	10.1		9.63	10.35
High-Temperature Cap	Substrate Temp (°C)	580	595	595	585	580
	As (%)	55	55	55	55	55
	Growth Rate(ML/s)	0.611	0.638		0.62	
	Time (sec)	496	496	496	496	496
	Thickness (ML)	303.06	316.60		308.39	
	Thickness (nm)	85.85	89.68		87.36	
	Total Thickness (nm)	98.81	99.4	~100	96.99	~100

TABLE 3.2. In$_{0.4}$Ga$_{0.6}$As quantum dot sample details of GaAs thin cap.

			Thin Cap QD Samples			
	Sample	F	G	H	I	J
	Serial #	030607-1	030607-2	030907-1	030907-2	022807
Buffer	Moly/Plate	l/o	u/u	n	o	u
	Growth Temp(^{0}C)	575	590~595	595	575	
	Growth Rate(ML/s)	0.62	0.66	0.66	0.67	0.63
	Growth Time	2hr 3 min	2hr 12 min	1hr 40 min	3hr 25 min	
	Thickness (nm)	1294.9	1477.1	1112.2	2314.8	
QD Layer	Growth Temp(^{0}C)	350	370	370	360	370
	As (%)	100	12	15	20	40
	Growth Rate(ML/s)	0.21	0.22	0.211	0.21	
	Growth Time (sec)	70	70	47	47	70
	Thickness (ML)	15.00	15.00	9.94	10.00	
	Thickness (nm)	4.24	4.25	2.81	2.83	
Annealing	Temp (^{0}C)	480	490	470	480	450
	Time (sec)	120	120	120	120	120
RHEED	Q Dot	Y	Y	N	Y	Y
Low-Temperature Cap	Substrate Temp (^{0}C)	480	490	500	480	450
	As (%)	100	12	15	20	40
	Growth Rate(ML/s)	0.22	0.19	0.12		
	Time (sec)	160	160	160	160	160
	Thickness (ML)	35.29	30.19	19.84		
	Thickness (nm)	10.00	8.55	5.61		
	Total Thickness (nm)	10.00	8.55	5.61	~10	~10

FIG. 3.5. AFM image of sample A. The image size is 3×3 μm. 11.9 ML of InGaAs QD are grown at 350^0C and a 100 nm GaAs cap layer is deposited.

FIG. 3.6. AFM image of sample B. The image size is 20×20 μm. 9.47 ML of InGaAs QD are grown at 360^0C, and a 100 nm GaAs cap layer is deposited.

FIG. 3.7. AFM image of sample C. The image size is 10×10 μm. 9.49 ML of InGaAs QD are grown at 360^0C, and a 100 nm GaAs cap layer is deposited. No QDs are observed.

FIG. 3.8. AFM image of sample D. The image size is 40×40 μm. 10 ML of InGaAs QD are grown at 350^0C, and a 100 nm GaAs cap layer is deposited.

FIG. 3.9. AFM image of sample E. The image size is 30×30 μm. 7.3 ML of InGaAs QD are grown at 360^0C, and a 100 nm GaAs cap layer is deposited.

FIG. 3.10. AFM image of sample F. The image size is 3×3 μm. 15 ML of InGaAs QD are grown at 350^0C, and a 10 nm GaAs cap layer is deposited.
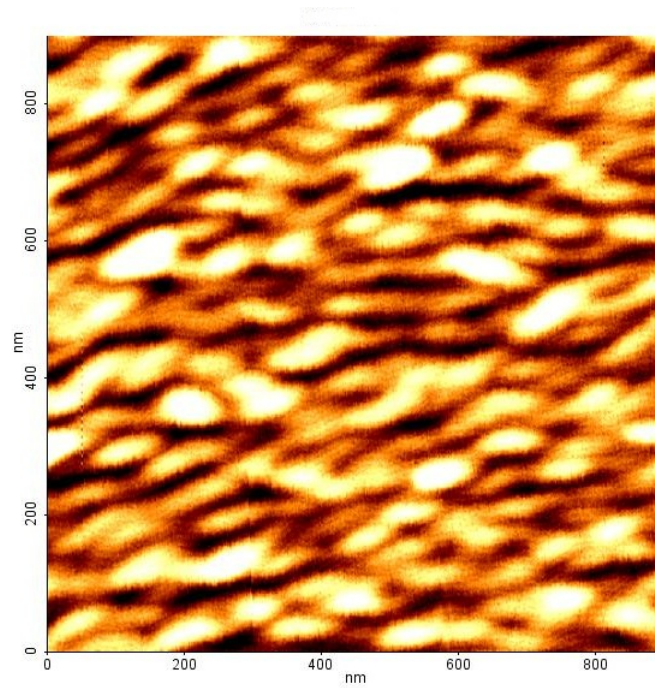
FIG. 3.11. AFM image of sample G. The image size is 0.9×0.9 μm. 15 ML of InGaAs QD are grown at 370^0C, and a 10 nm GaAs cap layer is deposited.
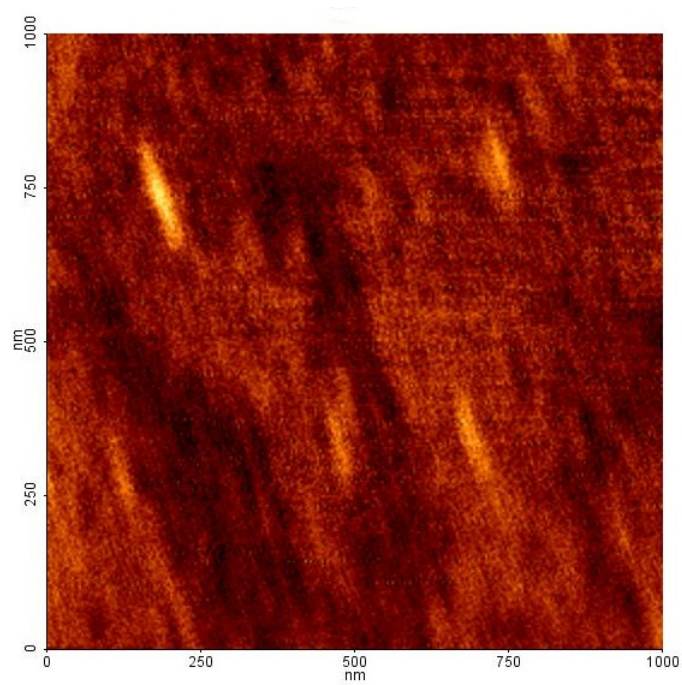
FIG. 3.12. AFM image of sample H. The image size is 1×1 μm. 10 ML of InGaAs QD are grown at 370^0C, and a 10 nm GaAs cap layer is deposited. No QD observed.
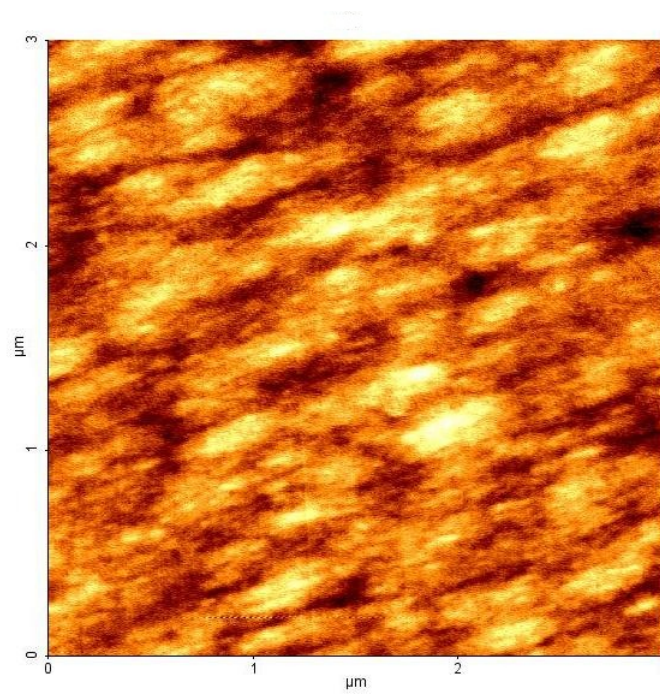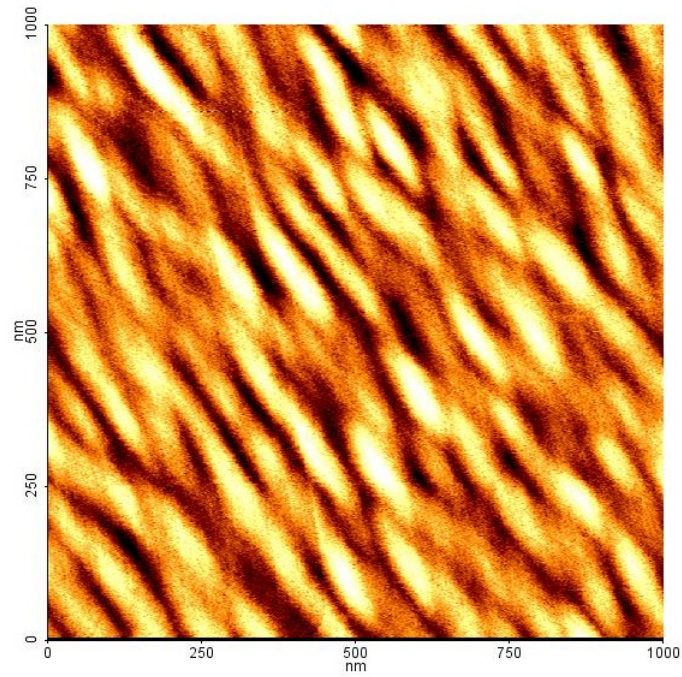
FIG. 3.13. AFM image of sample I. The image size is 1×1 μm. 10 ML of InGaAs QD are grown at 360^0C, and a 10 nm GaAs cap layer is deposited.
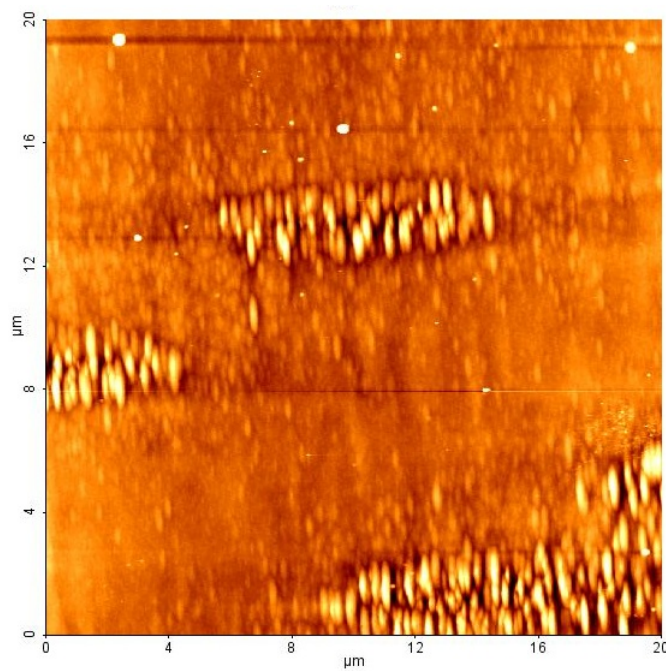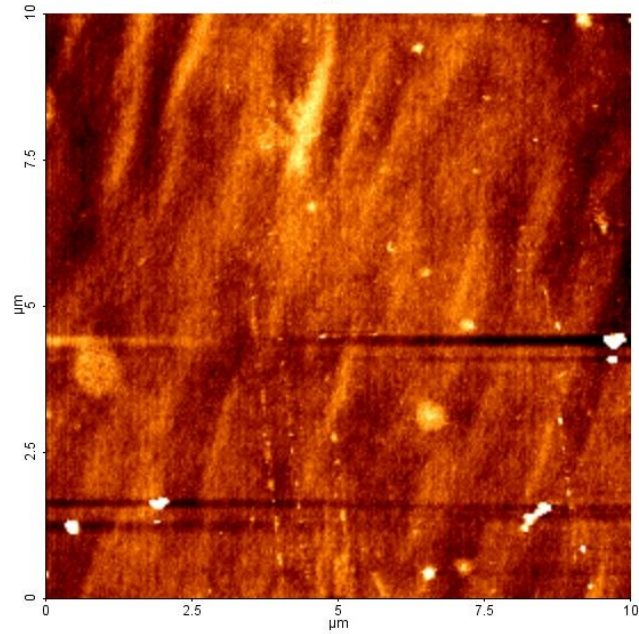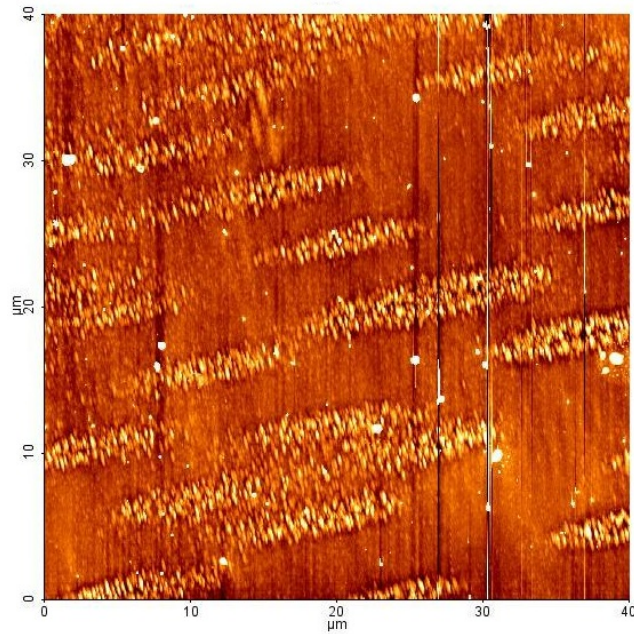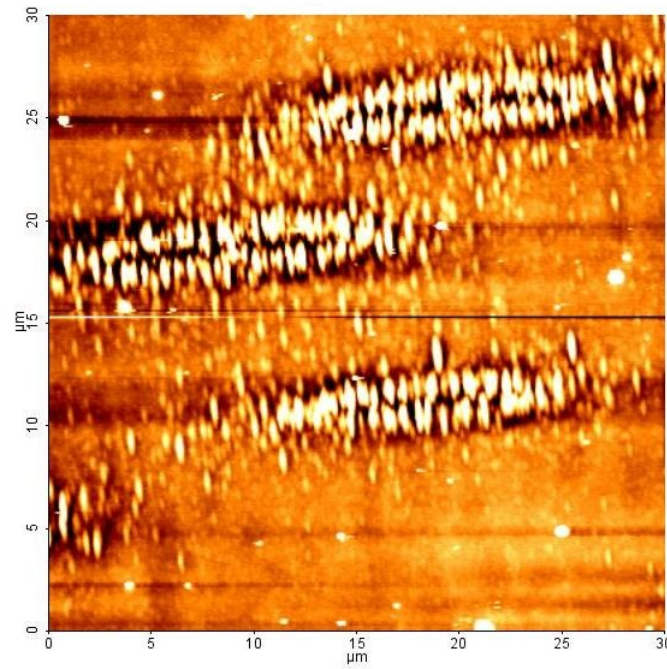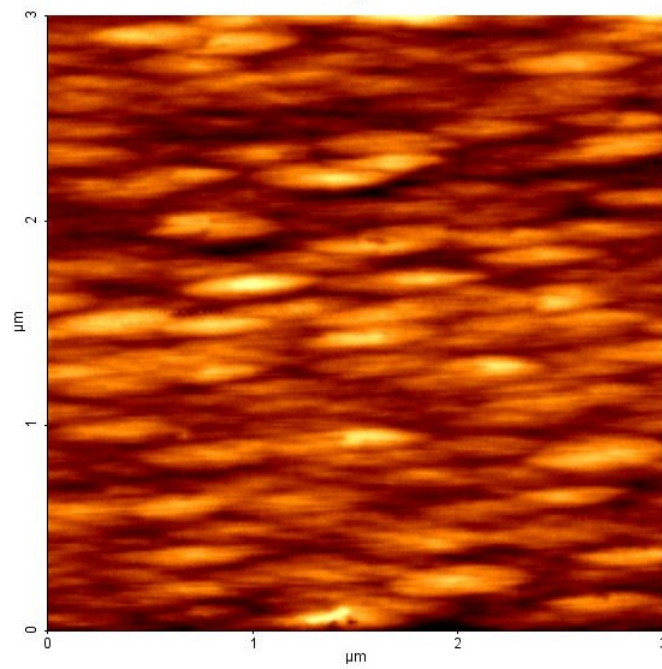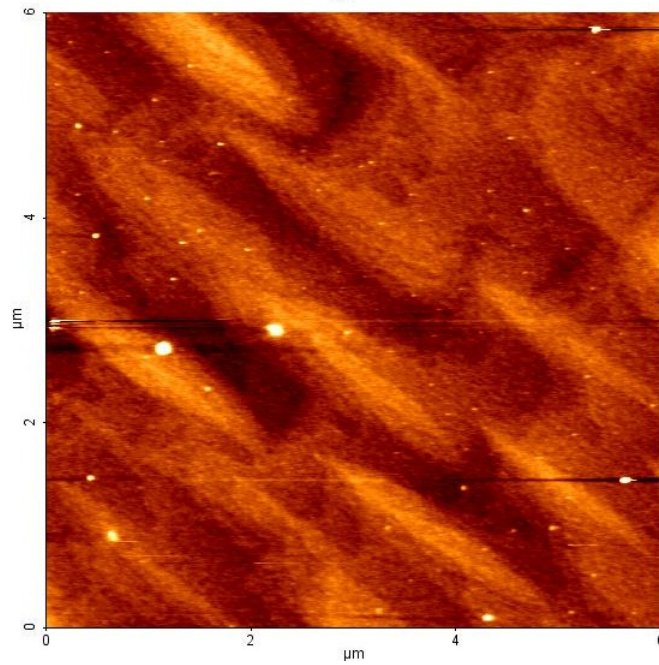

FIG. 3.14. AFM image of sample J. The image size is 6×6 μm. InGaAs QD are grown at 370^0C, and a 10 nm GaAs cap layer is deposited.

CHAPTER 4

REFLECTIVITY MEASUREMENTS

One of the most common ways of growing InGaAs QDs is by Stranski-Krastanov growth. Yang and coworkers have used the modified SK growth mode as explained in section 3.4.1. In this growth mode, elastic energy associated with the lattice mismatch strain between different epitaxially deposited semiconductor layers is minimized through the formation of small QDs connected via a thin wetting layer (WL). These QDs are typically of pyramidal shape with ~25-nm base dimension, and ~8-nm height, and further these QD samples are capped with GaAs layer of 10 or 100 nm.

Carrier capture into QDs and their relaxation has been an interesting topic of investigation in the last decade. Slow relaxation rates are attributed to the phonon bottleneck [47]. On the other hand, several mechanisms have been proposed to describe the faster relaxation processes, Auger processes [28, 35, 58], electron-hole scattering [37, 50], and multiphonon emission [59, 60]. Relaxation times depend on the number of factors, such as the size of the QDs, excitation level, lattice temperature, ground-state energy, and annealing temperature.

In this chapter, we study the carrier dynamics in InGaAs QDs using time-resolved pump-probe reflectivity.

4.1 Thick Cap QDs

4.1.1 Reflectivity Data

We have made ultrafast measurements on InGaAs QD samples using nearly Gaussian pulses of 25 fs from our home-built Ti-sapphire laser at 800 nm. We have done three different total-time-delay scans on all of our QD samples: 5ps, 25 ps, and 120 ps. For each total time delay we have used seven different neutral density filters to collect the data over the range of different laser intensities. The range of relative intensities goes from 100% down to 2.4%.

Data from all of the thick samples look similar to the data from sample A shown in Fig. 4.1. Figure 4.1 shows the time-dependent reflectivity response of sample A over the range of laser intensities. Data taken with total delay of 5 ps is shown in the left panel. A step size of 13.3 fs was used. For all the data, the initial reflectivity change is positive. For all but the two lowest intensity scans, the reflectivity response decays past the baseline. Figure 4.1 also shows the time resolved reflectivity ($\triangle R/R$) for scans of 25 ps and 120 ps with step sizes of 66.7 fs and 333.5 fs, respectively. As the data in Fig 4.1 illustrate, even by 120 ps, the reflectivity has not necessarily recovered to its initial value.

Figure 4.2(a) and (b) illustrate the reflectivity of thick-cap QD samples verses the time delay when the relative laser intensity is 0.65 and 0.13, respectively. For all the thick-cap samples, the initial reflectivity is positive, and they are arranged in order of increasing annealing temperatures (from bottom to top). Reflectivity of these samples does not cross the baseline except for samples C and A at both the laser intensities. These data show little variation in the initial reflectivity drop among the samples. Also the reflectivity does not recover to its initial point. Even for our maximum time-delay scan of 120 ps, the reflectivity has not fully recovered. This has also been observed by other groups [61, 62].

4.1.2 Modeling and Analysis of QD samples

Our analysis methodology is based on the following assumptions: (i) the carrier distribution can be described by a set of time-dependent density components, (ii) the excitation and relaxation of the carriers can be described by a set of first-order, linear rate equations for these density components, and (iii) the reflectivity can be expressed as a linear combination of these components. These assumptions are consistent with a description of the reflectivity being described by a linear combination of decaying exponential functions,

$$\frac{\triangle R}{R}(t) = \sum_j \bar{\Theta}_j(t) A_j exp(-\frac{t}{\tau_j}), \tag{4.1}$$

38

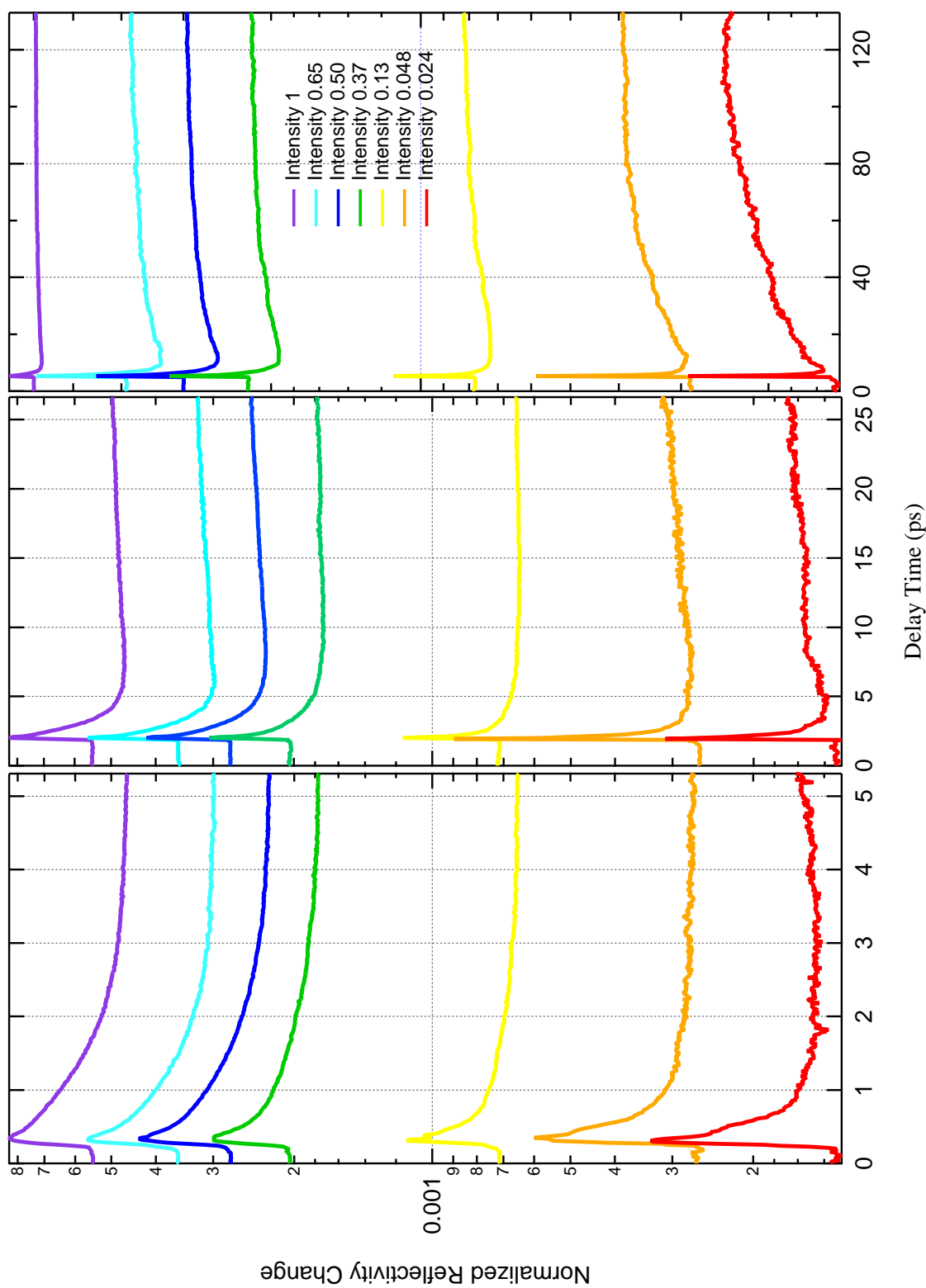FIG. 4.1. Normalized reflectivity of QD sample A vs. time delay for 5-ps scan, 25-ps scan, and 120-ps scan.
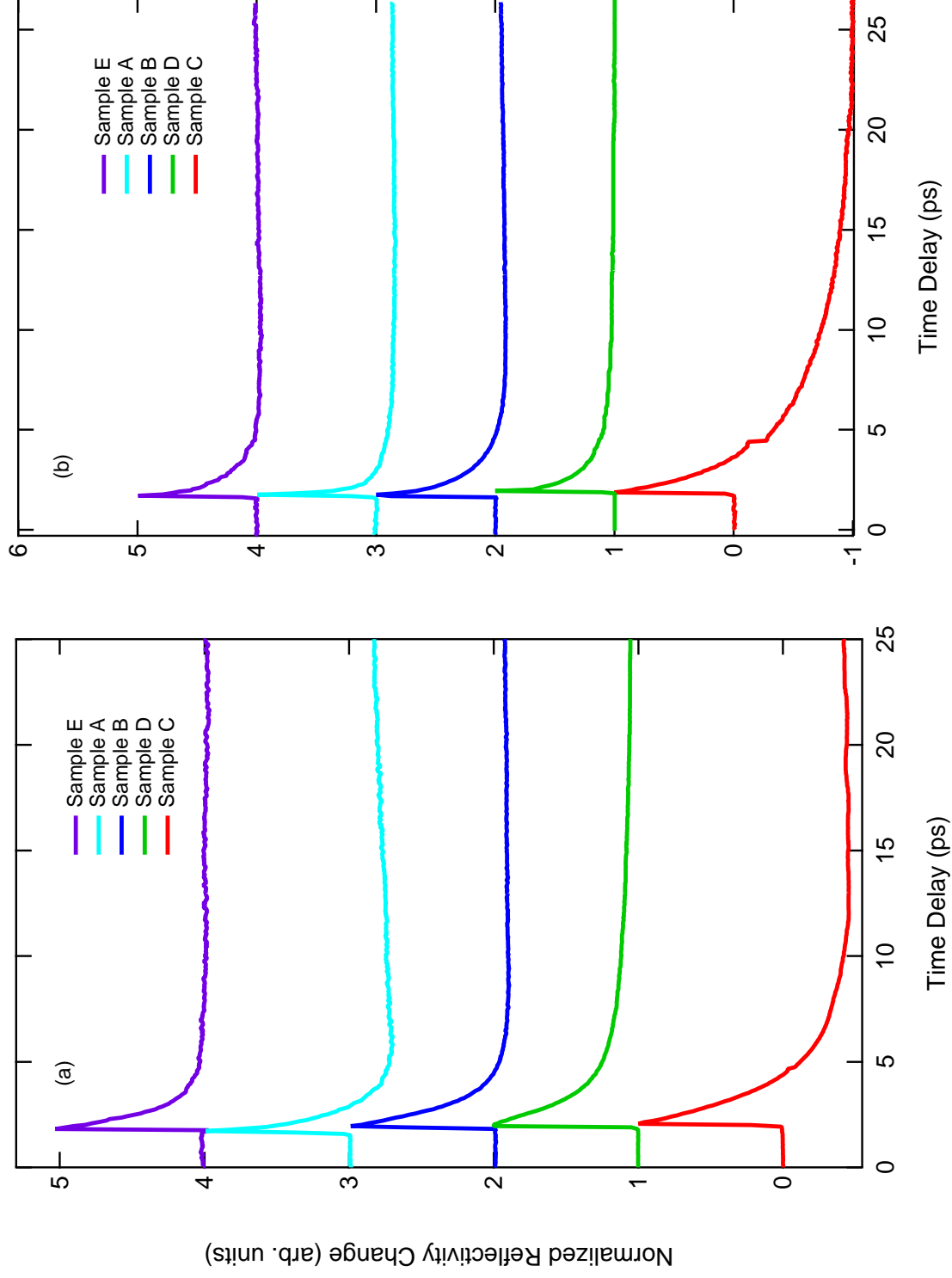
FIG. 4.2. Normalized reflectivity change vs. time delay for thick-capped quantum dot samples. Data from samples A, B, C, D, and E are displaced for clarity and arranged in order of increasing annealing temperature (from bottom to top) (a) when laser intensity was 0.65 and (b) when laser intensity was 0.13.

39

where τ_j are decay constants associated with relaxation processes of the carriers. The function

$$\bar{\Theta}_j(t) = \frac{1}{2}exp\left(\frac{\tau_p^2}{4\tau_j^2}\right)\left[erf\left(\frac{t}{\tau_p} - \frac{\tau_p}{2\tau_j}\right) + 1\right], \tag{4.2}$$

accounts for the finite-time excitation by the pump laser pulse with pulse width τ_p.

Using equation 4.1, we have fit the InGaAs reflectivity data with least-squares analysis. Something unique about our data analysis is that we have joined three of our ps scans into one data set, as shown in Fig. 4.3. Each scan has a different step size. We have shown in Fig 4.3 a fit of highest intensity spectrum of Sample A. The solid blue line, which passes through the red data points is the overall fit. The four individual curves with different time constants are slightly displaced for clarity. τ_1 is the fastest timescale, which has a positive amplitude, and τ_2 is the second fastest and also has a positive amplitude. However, τ_3 and τ_4 are the longest timescales and have negative amplitudes. In the case of sample D, we used only three decay constants instead of four.

Figure 4.4 shows the least-squares fitting of reflectivity data of sample A for laser intensity at 0.5. It shows the reflectivity decays slower than at maximum laser intensity. Capture time and the longest relaxation time are sightly longer than at maximum laser intensity.

Figure 4.5 shows the reflectivity data of our lowest laser intensity (0.048) for sample A. It tells us the capture time, τ_2, and relaxation time, τ_3, increase from laser intensity 1 and 0.5.

The relaxation times τ_1, τ_2, and τ_3 are extracted from the analysis and are related to specific aspects of the carrier dynamics: τ_1 is the momentum and /or energy relaxation rate [15, 16, 18] , τ_2 is the capture time of carriers by the InGaAs layer, and τ_3 is the carrier relaxation rate within the layer. The term with $\tau_4 = \infty$ is used to describe the nonzero offset that is still present at the end of the 120-ps scan.

Tables 4.1 to 4.4 summarize our results of least-square fits of Samples A, B, D, and E.

41

FIG. 4.3. Normalized reflectivity data from Sample A. Blue curve shows the fit through the red data points. Four individual terms τ_1, τ_2, τ_3, and τ_4 are shifted for clarity. These are the part of fit curve. This data was obtained at highest laser intensity.
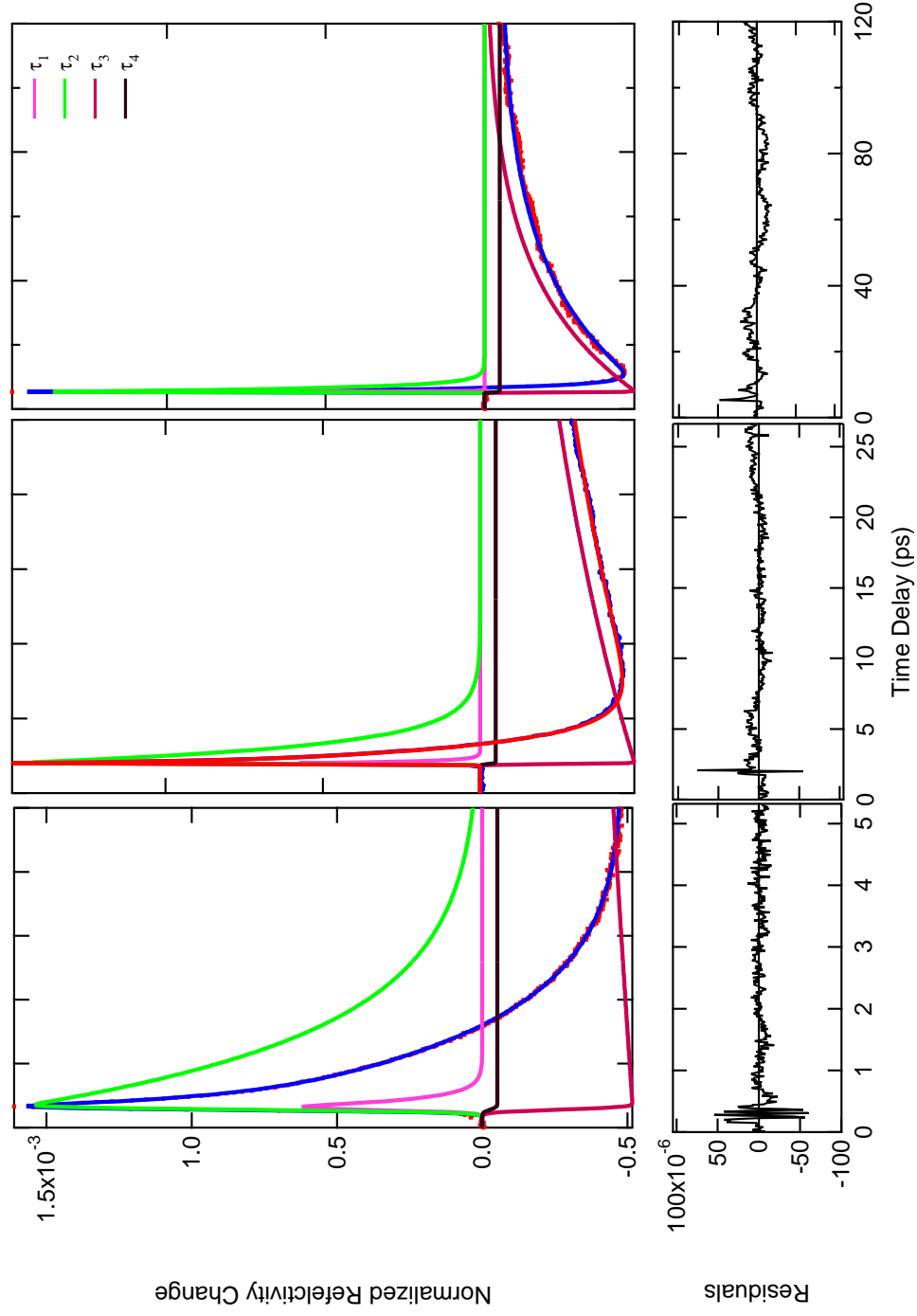
FIG. 4.4. Normalized reflectivity data from Sample A. Blue curve shows the fit through the red data points. Four individual terms τ_1, τ_2, τ_3, and τ_4 are the those are the decay constant. This data was obtained at laser intensity 0.50.
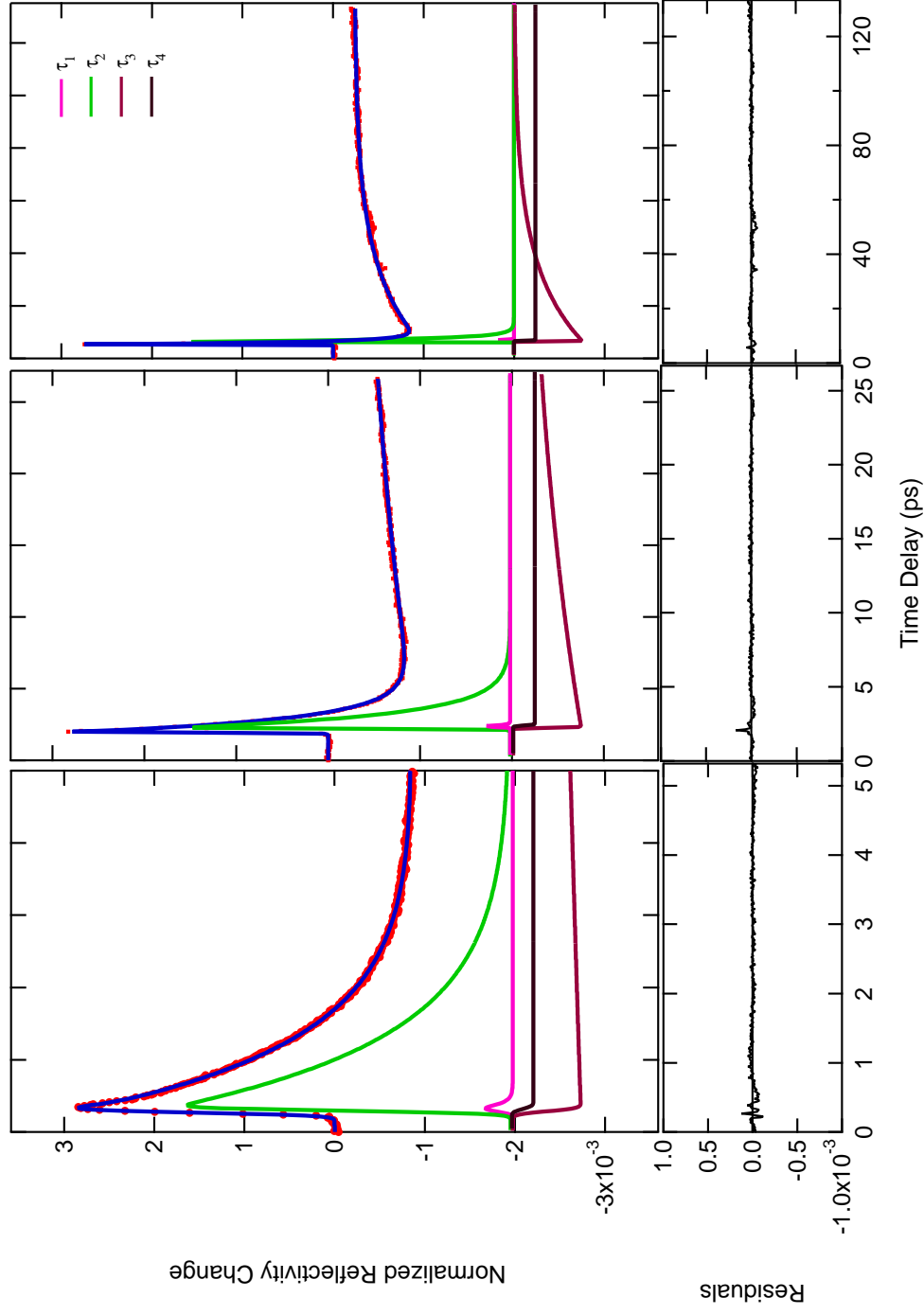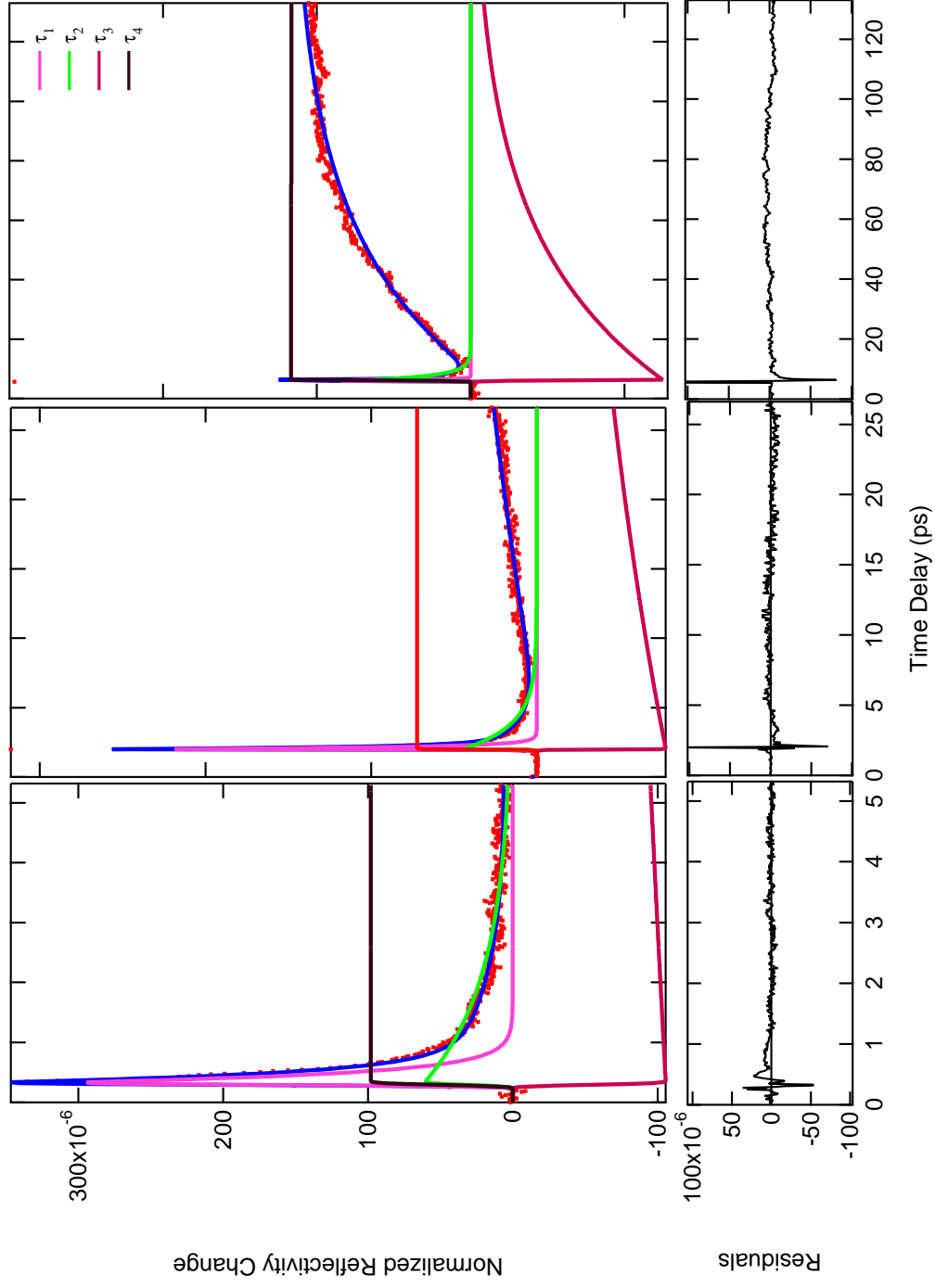
FIG. 4.5. Normalized reflectivity data from Sample A. Blue curve shows the fit through the red data points. Four individual terms τ_1, τ_2, τ_3, and τ_4 are the decay constant. This data was obtained at laser intensity 0.048.

For all four samples, τ_2 is typically between 1 and 2 ps for all laser intensities.

TABLE 4.1. Sample A different timescale for different intensity.

Intensity	0.048	0.13	0.38	0.50	0.65	1
τ_1(ps)	0.17	0.18	0.17	0.12	0.07	0.06
τ_2(ps)	1.723	2.51	1.76	1.20	0.96	1.02
τ_3(ps)	47.37	71.53	52.04	34.20	32.96	28.09

TABLE 4.2. Sample E different timescale for different intensity.

Intensity	0.024	0.048	0.13	0.38	0.50	0.65	1
τ_1(ps)	0.023	0.032	0.133	0.064	0.010	—	0.162
τ_2(ps)	1.01	1.1	1.27	0.89	0.79	0.8, 5.6	1.1
τ_3(ps)	302.12	102.24	144.82	97.8	29.6	17.6	1.8

TABLE 4.3. Sample B different timescale for different laser intensity.

Intensity	0.024	0.048	0.13	0.38	0.50	0.65
τ_1(ps)	0.239	0.180	0.182	0.637	0.215	—
τ_2 (ps)	1.91	1.836	1.73	1.040	1.13	1.3
τ_3 (ps)	43.53	32.23	31.99	56.58	108.71	41.2

TABLE 4.4. Sample D different time scale for different laser intensity.

Intensity	0.024	0.048	0.13	0.38	0.50	0.65	1
τ_2 (ps)	0.97	1.13	1.21	1.11	1.09	1.37	1.27
τ_3 (ps)	4.8	4.73	7.41	10.95	9.1	11.36	14.78

Figure 4.6(a) plots the capture time, τ_2, of the thick QD samples as a function of laser intensity. As the graph indicates, for sample E, τ_2 is approximately constant at ~1 ps versus laser intensity. Similarly, for sample D, the capture time, τ_2, is ~ 1.1 ps at all laser intensities. For sample B, the capture time, τ_2, varies from ~ 1.9 ps to ~ 1.3 ps as the laser intensity is increased. For sample A, the capture time, τ_2, varies from ~ 1.7 ps to ~ 1.0 ps as the laser intensity is increased.
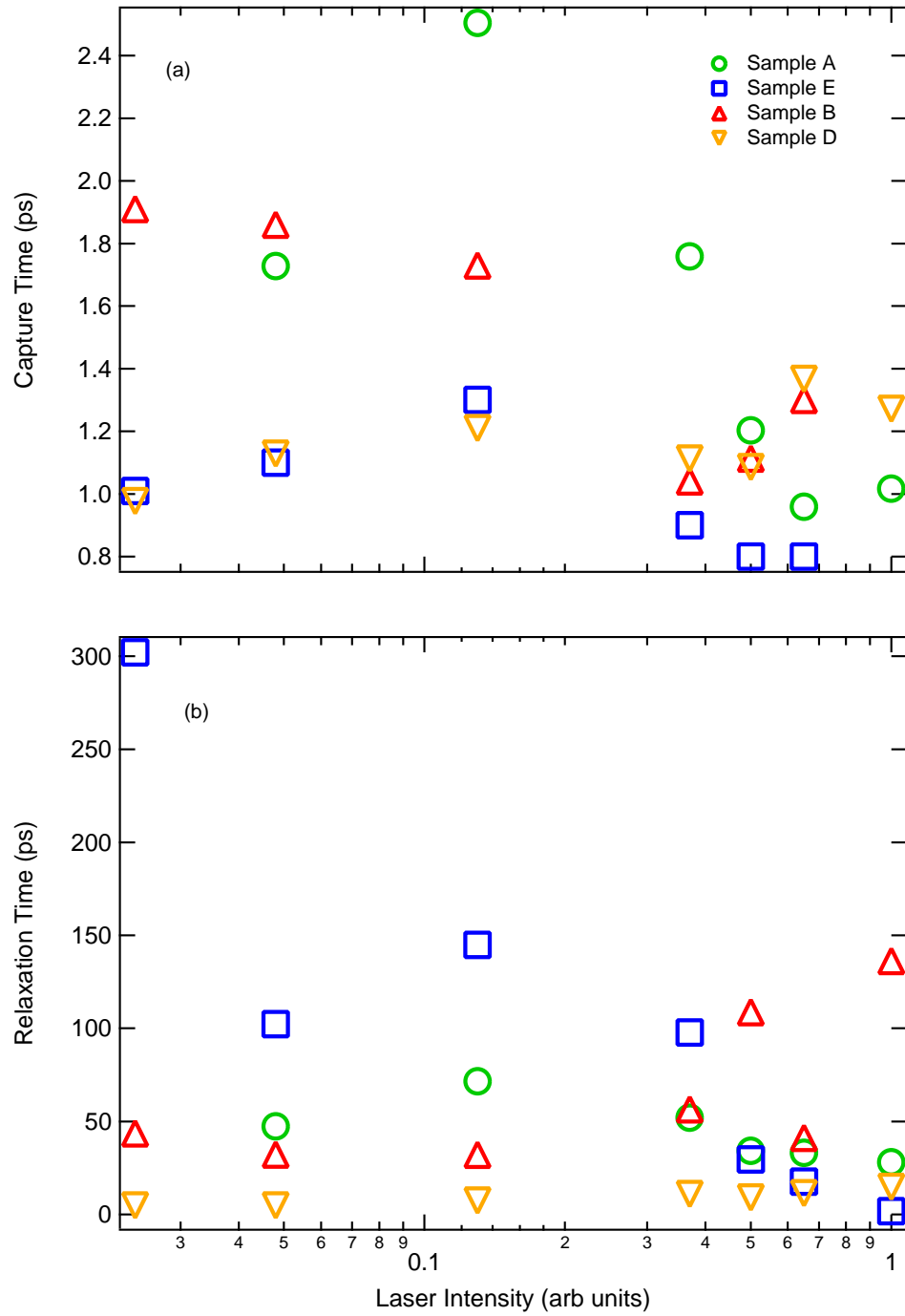
FIG. 4.6. Symbols are the results to least-square fitting of reflectivity data on InGaAs QDs. a) Capture times (τ_2) vs. laser intensity for samples A, B, D and E. b) Longest relaxation time (τ_3) vs. laser intensity.

Figure 4.6(b) shows the relaxation time, τ_3, of thick InGaAs QD samples as a function of laser intensity. For sample B, the longest relaxation time, τ_3, varies from ~ 40 ps to ~ 100 ps as the laser intensity is increased. For sample D, this relaxation time varies from ~ 4 ps to ~ 14 ps as the laser intensity is increased. For sample A, τ_3 varies from ~ 50 ps at lowest intensity to ~ 30 ps at highest intensity. For sample A, τ_3 varies from ~ 4 ps to ~ 14 ps as the laser intensity is increased. Lastly, for sample E, the longest relaxation time, τ_3, decreases from ~ 300 ps to ~ 17 ps as the laser intensity is increased. As the graph shows, there is no consistent trend in τ_3 versus laser intensity among the samples.

4.1.3 Discussion

In the experiment, electrons are excited into the GaAs barrier under 800-nm laser excitation because the photon energy is larger than the band gap of GaAs. Electrons then quickly relax into lower energy levels of the GaAs barrier and then into the InGaAs WL via electron-phonon and electron-electron scattering [63]. Electrons then relax to the lower-energy states associated with the QDs. Phonon scattering is the most dominant mechanism for relaxation within the InGaAs QDs due to the close separation of the hole levels and the availability of various energy-broadened phonons [32]. In this case, a perfect match between the inter-subband and LO phonon energies is not critical for a fast-carrier relaxation. A fast-carrier relaxation is possible even through multiphonon relaxation involving optical and acoustic phonons [64, 65].

Figure 4.1 shows the longest timescan of 120 ps in which the reflectivity does not recover to its initial point suggesting the carriers are still hot and not yet fully relaxed. This longest timescale corresponds to the Auger relaxation time. As indicated by our longest 120-ps scan, Auger processes work effectively as there are many carriers, since an electron can find an electron or hole into which to transfer its energy and thus fall into the QD energy levels. This process helps trapped carriers to relax further to the lowest energy in QDs.

Another possible mechanism for slower relaxation times is the state-filling effect. Raymond and coworkers have studied the state-filling effect in InGaAs quantum dot structures, and give detailed information about the carrier dynamics [66, 67, 68]. The Pauli exclusion principle becomes effective when few carriers are present in the lower states. Phonon bottleneck, state filling and segregated inhomogeneous broadening can give rise to higher-energy emission peaks, but they possess different characteristic features. The state filling effect is the only one that will show clear saturation effects. At low intensities, the ground-state levels are observed. The Phonon bottleneck effect is not observed because of the faster inter-sublevel relaxation, as compared to interband recombination.

With further increase of laser intensity, however, the capture times do not show a further decrease. At low-laser intensity, the electron states of the QDs are almost empty and therefore, the state-filling effect plays an insignificant role. On the other hand, the density of excited electrons in the WL is very low so the probability of electron-hole scattering is very low, and thus a long capture time is observed. With increasing laser intensity, the density of excited electrons increases and thus electron-hole scattering is enhanced, which leads to a decrease of the capture time. With increasing laser intensity, however, the density of electrons in the QD states increases, as well. The state-filling effect begins to play an increasing role. With further increase of laser intensity, the state filling effect becomes the dominant mechanism, and thus the capture time does not shorten further, but rather, increases.

No phonon bottleneck is observed in our experiments. The main relaxation mechanisms are phonon or multiphonon scattering. An increasing density of electron-hole pairs leads to an increase of the probability of electron-hole scattering, which results in a decrease of the capture time. At high excitation levels, the state-filling effects produces the increase of capture time.

For sample E, the longest relaxation time, τ_3, decreases from ~ 300 ps at the minimum

intensity to ~ 1.8 ps at maximum intensity. Similarly, in sample A the relaxation time, τ_3, decreases from ~ 50 ps to ~ 28 ps as the laser intensity is increased. The results for these two samples suggest carrier-carrier scattering controls the relaxation. On the other hand, τ_3 for the samples B and D do not appear to systematically vary versus laser intensity. As for τ_2, all values lie between 0.8 and 2.5 ps, with no systematic variation versus laser intensity.

4.2   Thin Cap QDs

4.2.1   Reflectivity Data

We have also measured the normalized reflectivity of the thin-cap QD samples as a function of time delay. Most of our data from the thin-cap samples look similar. Figure 4.7 shows time-dependent reflectivity curves from sample I obtained over a wide range of laser fluences. The laser intensity has been changed from 100% to 2.4%. This figure shows the reflectivity spectra have an initial positive response followed by a short decay to a positive value. The data in Fig. 4.7 suggest carrier capture is faster at lower excitation intensities.

Figure 4.8(a) and (b) illustrate the reflectivity of thin QD samples vs. the time delay of 25 ps when laser intensity is 0.65 and 0.13, respectively. For all the thin samples, initial reflectivity is positive and they are arranged in the order of their increasing annealing temperatures (from bottom to top). Reflectivity of these samples does not cross the baseline. These data suggest as the annealing temperature increases, the reflectivity of these samples decays faster. As with the thick-cap samples, even at our maximum time delay scan of 120 ps, the reflectivity has not necessarily fully recovered.

4.2.2   Results and Analysis

Using Eq. 4.1, we have again fit the combined short-, medium-, and long-timescale reflectivity data with least-squares analysis. Figure 4.9 shows the reflectivity fit of sample I. The normalized reflectivity change is positive for all of our scans. τ_1 is the fastest timescale
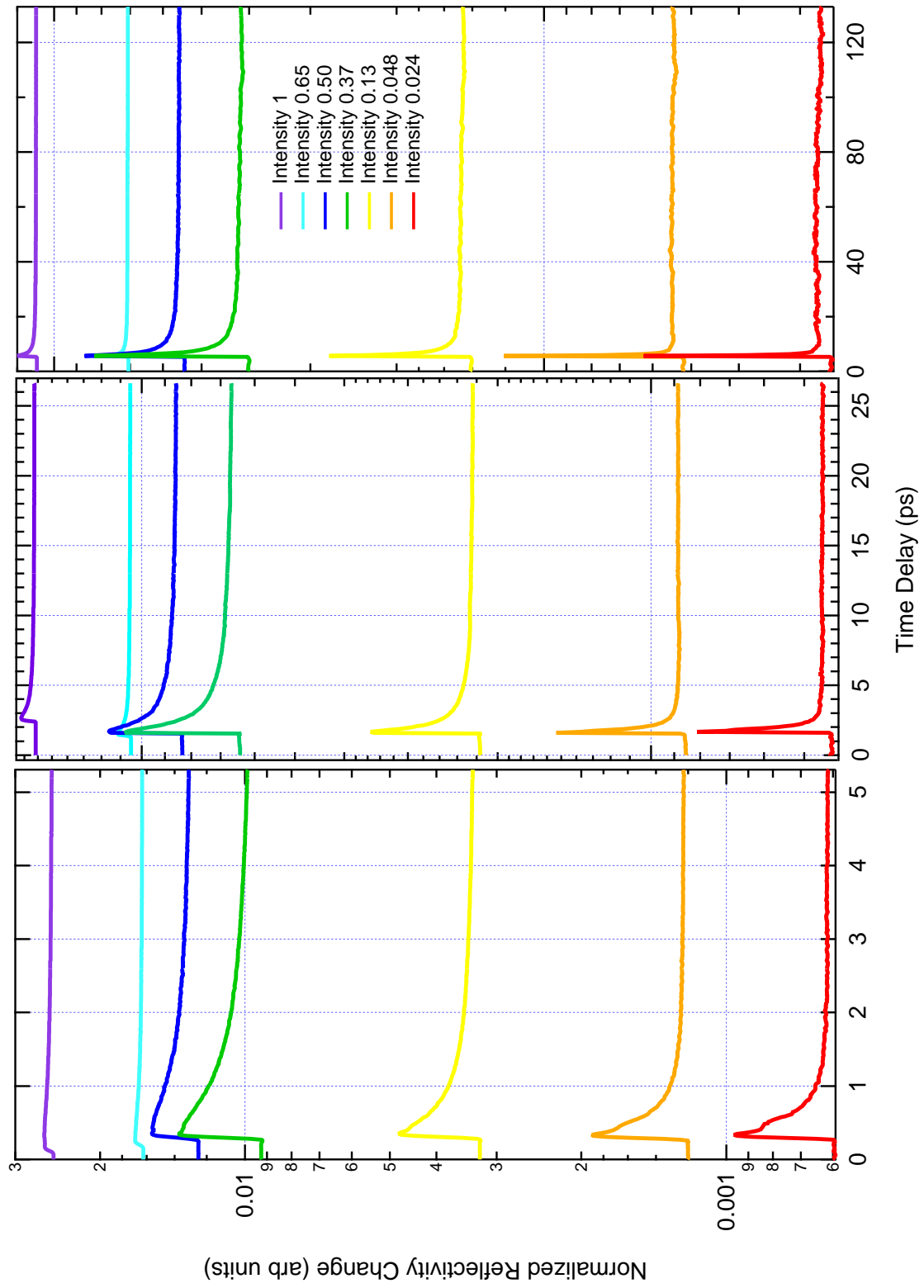
FIG. 4.7. Normalized reflectivity of QD sample I vs. time delay (ps) for 5-ps scan, 25-ps scan, and 120-ps scan.
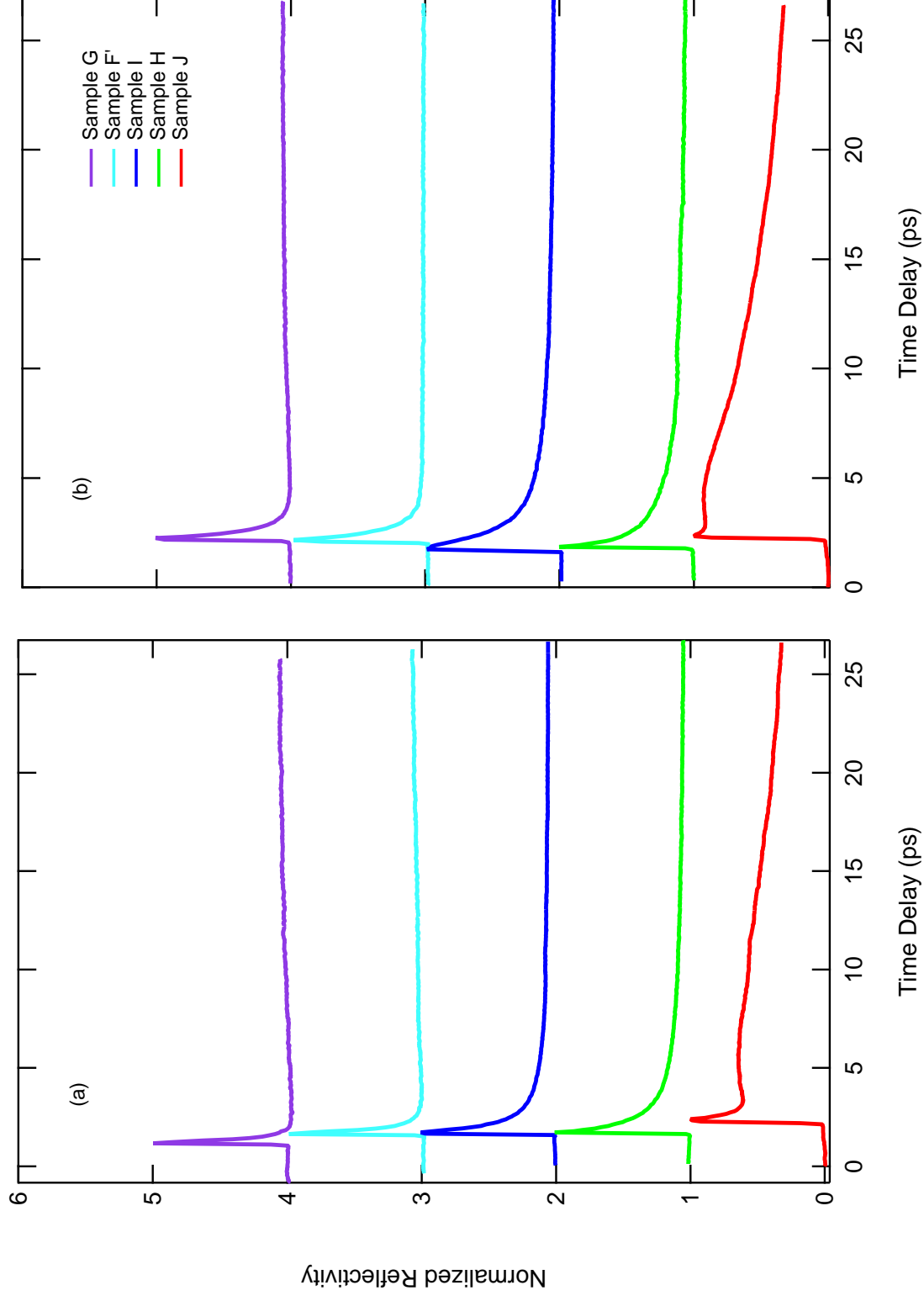
FIG. 4.8. Reflectivity data vs. time delay. Data from sample F, G, H, I, J are displaced for clarity and arranged in the order of decreasing annealing temperature (a) when laser intensity was 0.13, and (b) when laser intensity was 0.65.

50

and has a negative amplitude, but τ_2 and τ_3 are longer timescales with positive amplitudes. The blue curve shows the overall fit of the data comprised of all three time constants. The red dots represent the data points.

Figure 4.10 shows the reflectivity fit of thin sample G at laser intensity 0.37. The normalized reflectivity change is positive for all our scans, and it passes the baseline. We have fit this sample using only three exponential functions: τ_2 is the fastest timescale and has a positive amplitude; τ_3 is a longer timescale and has a negative amplitude; τ_4 is again set to ∞. The blue curve shows the overall fit of data, which is comprised of all three time constants. Again the red dots represent the data points.

Figure 4.11 shows the reflectivity fit of thin sample F at laser intensity 0.13. Normalized reflectivity change is positive for all our scans, and in this case, it does not pass the baseline. We have also fit this sample using the three exponential functions. Again, τ_2 is the fastest timescale and has a positive amplitude; τ_3 is a longer timescale with a negative amplitude; τ_4 is again set to ∞. The blue curve shows the overall fit of the data is comprised in all three time constants. The red dots represent the data points.

Results of our least-squares analysis of reflectivity data from samples F, G, and I are summarized in Tables 4.5 to 4.7. As for the thick samples, we identify τ_2 with carrier capture by the InGaAs layer and τ_3 with relaxation within the layer.

TABLE 4.5. Sample I different time scale for different laser intensity.

Intensity	0.024	0.048	0.13	0.38	0.50	0.65	1
τ_1 (ps)	0.18	0.16	0.31	0.84	0.96	0.85	1.3
τ_2 (ps)	0.47	0.59	1.65	4.73	5.72	6.23	7.9
τ_3 (ps)	441.79	417.49	157.5	163.7	178.64	274.2	181.7

FIG. 4.9. Normalized reflectivity data from sample I at full laser intensity. Blue curve shows the fit through the red data points. Residual of the fit is shown in bottom figure.

FIG. 4.10. Normalized reflectivity data from sample G at laser intensity 0.37. Blue curve shows the fit through the red data points. Residual of the fit is shown in bottom figure.
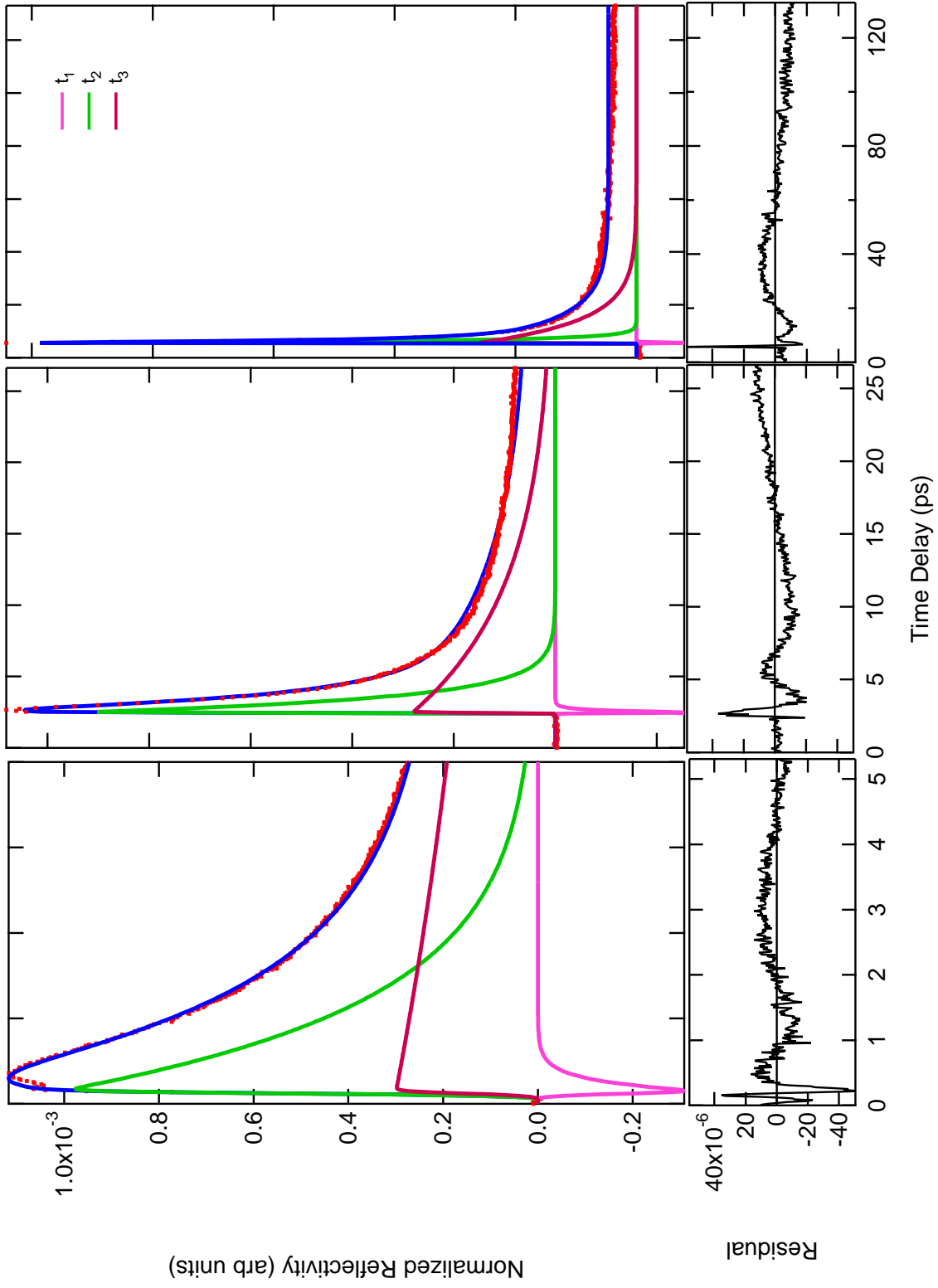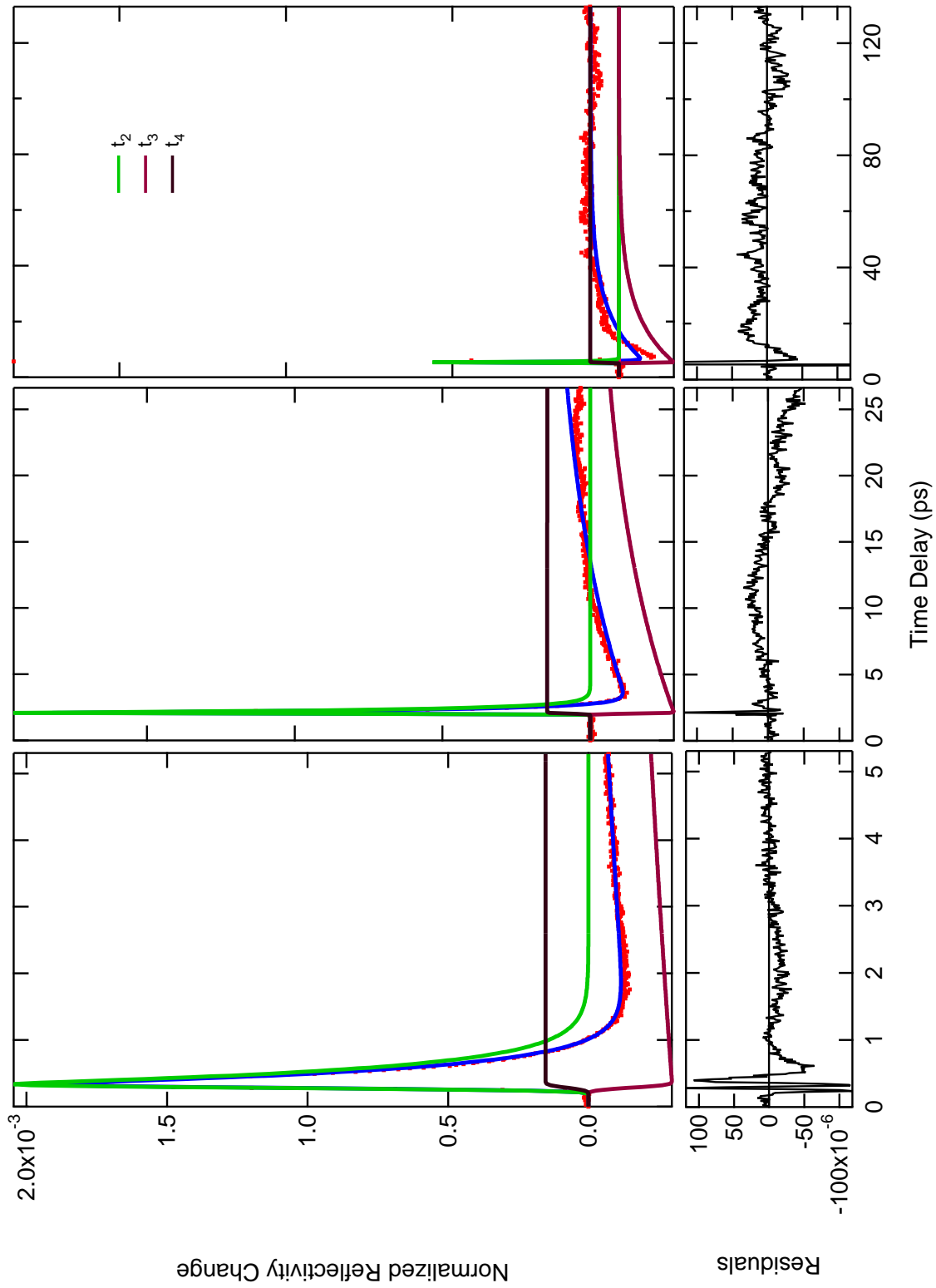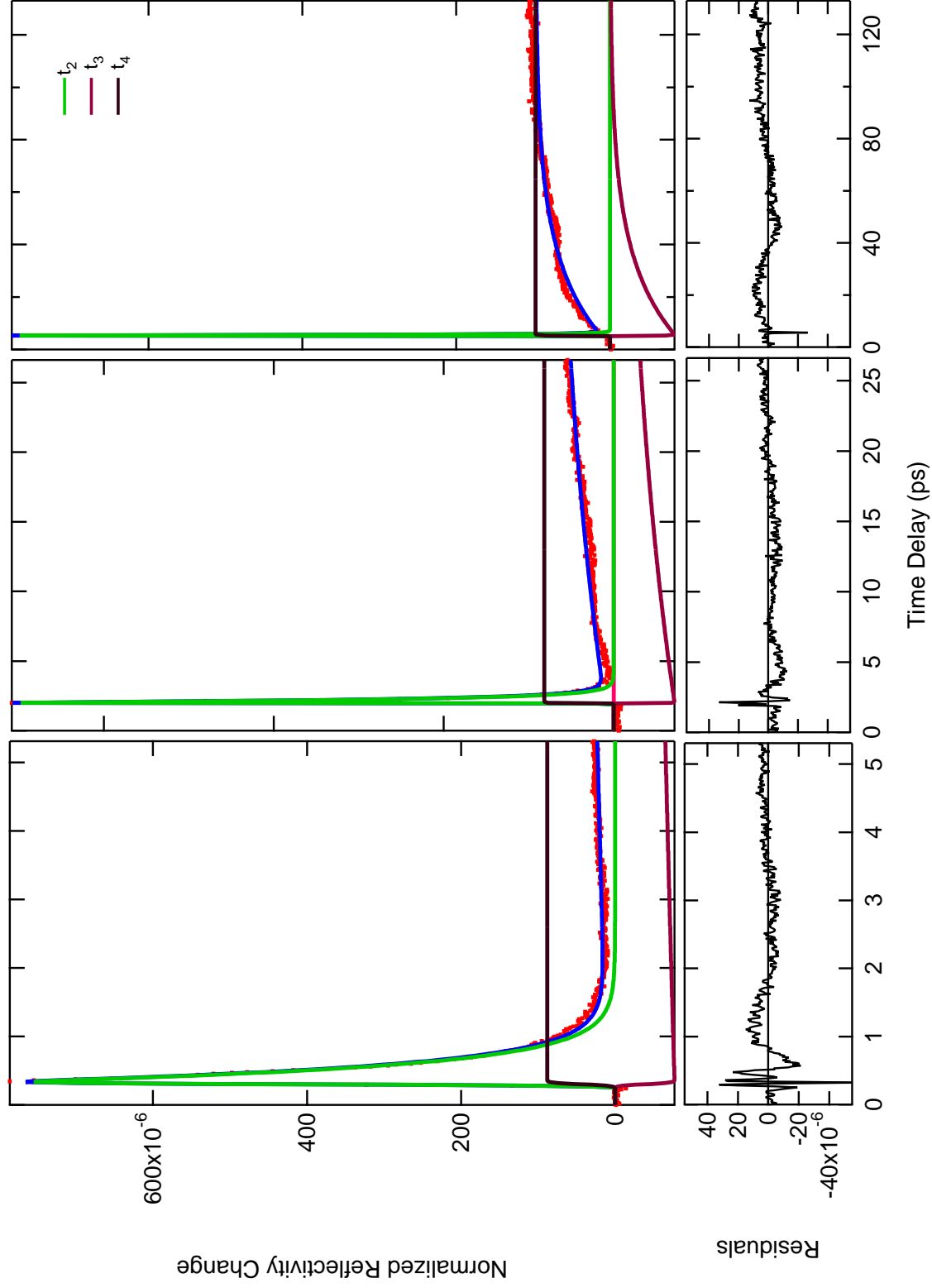
54

FIG. 4.11. Normalized reflectivity data from sample F at laser intensity 0.13. Blue curve shows the fit through the red data points. Residual of the fit is shown in bottom figure.

TABLE 4.6. Sample F different time scale for different laser intensity.

Intensity	0.024	0.048	0.13	0.38	0.50	0.65	1
τ_2 (ps)	0.25	0.27	0.25	0.38	0.34	0.45	0.60
τ_3 (ps)	59.0	78.379	30.01	44.84	23.74	16	16

TABLE 4.7. Sample G different time scale for different laser intensity.

Intensity	0.024	0.048	0.13	0.38	0.50	0.65	1
τ_2 (ps)	0.21	0.139	0.22	0.261	0.300	0.39	0.51
τ_3 (ps)	15.79	5.07	26.83	15.71	24.64	32.23	3.47

Figure 4.12(a) illustrates the capture time, τ_2, of thin-cap QD samples as a function of laser intensity. As the graph indicates, for sample I, τ_2 increase from ~0.46 ps to ~7.8 ps. For sample G, capture time, τ_2, increases from ~ 0.21 ps at lower laser intensities to ~ 0.51 ps at the highest intensity. For sample F, capture time, τ_2, varies from ~ 0.29 ps to ~ 0.6 ps as the laser intensity is increased. The general trend of τ_2 increasing with laser intensity can be attributed to the state filling.

Figure 4.12(b) plots the longest relaxation time, τ_3, of the thin-cap InGaAs QD samples as a function of laser intensity. For sample I, τ_3 varies from ~ 440 ps to ~ 180 ps as the laser intensity is increased. For sample G, τ_3 varies from ~ 15 ps to ~ 3 ps as the laser intensity is increased. For sample F, τ_3 decreases from ~ 59 ps at the minimum intensity to ~ 16 ps at highest intensity. The general trend of τ_3 decreasing with increasing laser intensity suggests carrier-carrier scattering is key to relaxation within the InGaAs layer.

Figure 4.13 plots the capture time, τ_2, versus annealing temperature for all thin-cap samples for each laser intensity. For full laser intensities, the capture time decreases from 1.1 ps to 0.4 ps. At laser intensity 0.65, capture time decreases from 0.49 ps to 0.37 ps as annealing temperature increases. At laser intensity 0.50, capture time increases 0.3 ps to 0.45 ps as annealing temperature decreases from 490^0C to 450^0C. At laser intensity 0.37, capture time decreases from 0.25 ps at 450^0C to 1.4 ps at 490^0C.
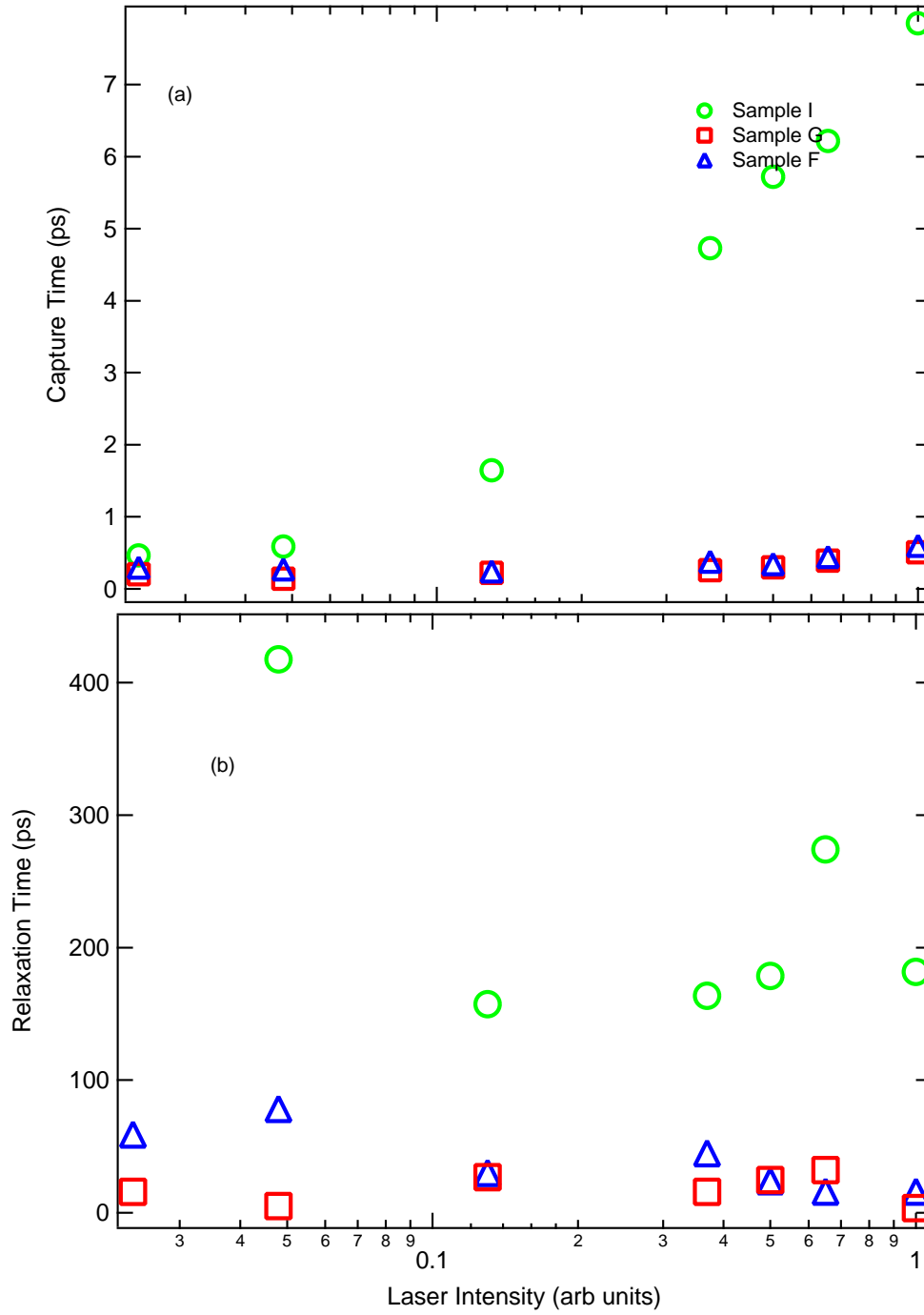
FIG. 4.12. Symbols are the results to least-square fitting of reflectivity data on InGaAs QDs. a) Capture times (τ_2) vs. laser intensity for samples F, G, and I. b) Longest relaxation time (τ_3) vs. laser intensity for samples F, G, and I.
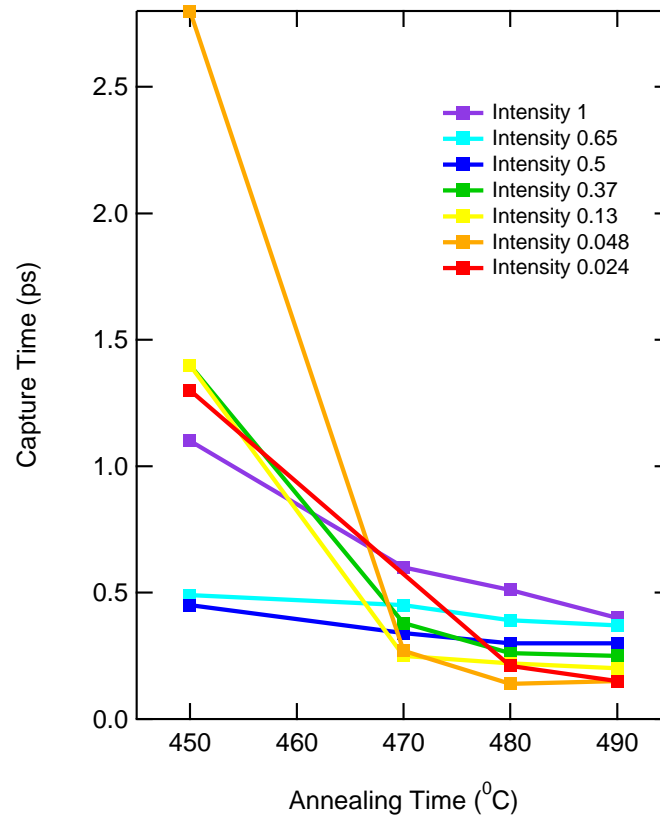
FIG. 4.13. Carrier capture time vs. annealing temperature are plotted for different laser intensities.

These data show a strong correlation of τ_2 with sample annealing temperature. As Yang and coworker have shown, higher annealing temperature result is QDs with wider bases and smaller heights. The results shown in Fig.4.13 thus indicate QD morphology affects carrier capture.

CHAPTER 5

TIME RESOLVED ELLIPSOMETRY

Ellipsometry is a technique used to characterize the optical properties of bulk materials, thin films, or even the interface between two media. It is based on exploiting the polarization transformation that occurs as a beam of polarized light is reflected from an interface or transmitted through a thin film. Ellipsometry is particularly attractive because of its ability to measure both the real (n) and imaginary (k) parts of the refractive index of a semiconductor. Ellipsometry was first used in 1889 by Drude for the characterization of thin film surfaces [69]. After the initial studies by Drude, the field of ellipsometry research was essentially dormant for nearly 75 years except for few occasional reports. One was as that of Tronstad [70], who was the first to demonstrate the power of this technique for electrochemical studies. In another Rothen [71] coined the word ellipsometry to distinguish such measurements of the change of the state of polarization of light upon reflection. With the advent of minicomputers in the late 1960s, there were numerous efforts on the automation of ellipsometers using various approaches. Because of its accuracy in measurements, ellipsometry is still widely used in industrial settings for the measurement of film thicknesses, which involves reflection from two interfaces.

5.1 Conventions

The widely accepted conventions in ellipsometry are those adopted at the 1968 Symposium on Recent Developments in Ellipsometry following discussions of a paper by Muller [72]. Briefly, the electric field of a monochromatic plane wave traveling in the direction of the z axis is taken as

$$E(z,t) = E_0 exp\left[i\left(\omega t - \frac{2\pi N}{\lambda}z\right)\right],\qquad(5.1)$$

where E_0 is a constant complex vector that represents the transverse electric field in the $z =$

0 plane, N is the complex refractive index of the optically isotropic medium of propagation, ω is the angular frequency, and t is the time. N is written in terms of its real and imaginary parts as $N = n - ik$, where $n > 0$ is the refractive index and $k \geq 0$ is the extinction coefficient. The positive directions of x and y before and after reflection form a right-handed coordinate system with the directions of propagation of the incident and reflected waves as shown in Fig. 5.1.
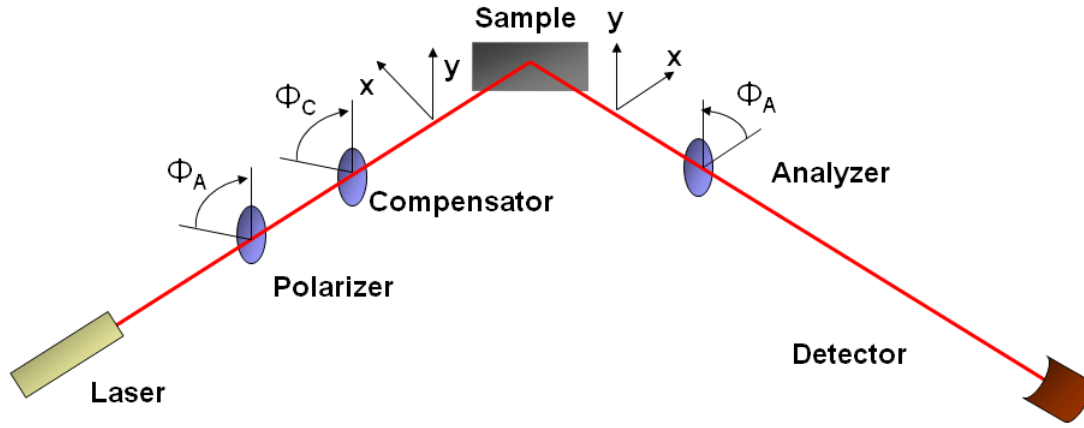
FIG. 5.1. PCSA Ellipsometer: represents the rotational azimuthal angles of polarizer, compensator and analyzer .

An ellipsometric measurement allows one to quantify the phase difference $\triangle$ between R_p and R_s, and the change in the ratio of their amplitudes, given by $\tan \psi$. The forms for Δ and ψ are

$$\Delta = \delta_p - \delta_s, \tag{5.2}$$

and

$$\tan \psi = \frac{|r_p|}{|r_s|}, \tag{5.3}$$

where, again, r_p and r_s are the Fresnel coefficients of p and s polarization. Ellipsometry

does not directly measure optical constants. It measures change in light polarization expressed as Δ and ψ. In ellipsometry, ρ is the ratio of complex reflection coefficients of the material for p and s polarizations, which can be expressed as

$$\rho = \frac{r_p}{r_s} = \tan \psi e^{i\Delta}. \tag{5.4}$$

The parameters Δ and ψ are used to calculate the refractive index of the material from which the light is reflected.

Equations 3.6 and 3.7 describe the reflection coefficients R_s and R_p, which give the ratio of reflected to incident intensity. These are the square moduli of the amplitudes r_s and r_p [73]. These reflection coefficients can also be written as

$$R_s = ||r_s|e^{i\delta_s}|^2 = \frac{a^2 + b^2 - 2a\cos\phi_0 + \cos^2\phi_0}{a^2 + b^2 + 2a\cos\phi_0 + \cos^2\phi_0}, \tag{5.5}$$

$$R_p = ||r_p|e^{i\delta_p}|^2 = R_s \left[\frac{a^2 + b^2 - 2a\sin\phi_0\tan\phi_0 + \sin^2\phi_0\tan^2\phi_0}{a^2 + b^2 + 2a\sin\phi_0\tan\phi_0 + \sin^2\phi_0\tan^2\phi_0} \right], \tag{5.6}$$

where

$$a = \sqrt{\frac{1}{2}\left[\left\{(n^2 - k^2 - \sin\phi_0)^2 + 4n^2k^2\right\}^{1/2} + (n^2 - k^2 - \sin^2\phi_0)\right]}, \tag{5.7}$$

$$b = \sqrt{\frac{1}{2}\left[\left\{(n^2 - k^2 - \sin\phi_0)^2 + 4n^2k^2\right\}^{1/2} - (n^2 - k^2 - \sin^2\phi_0)\right]}. \tag{5.8}$$

We can also write the reflection coefficients in terms of a and b as follows:

$$R_s = \frac{(a - \cos\phi_0)^2 + b^2}{(a + \cos\phi_0)^2 + b^2}, \tag{5.9}$$

and

$$R_p = R_s \frac{(a - \sin\phi_0 \tan\phi_0)^2 + b^2}{(a + \sin\phi_0 \tan\phi_0)^2 + b^2}, \tag{5.10}$$

and the phase changes upon reflection are given by

$$\tan\delta_s = \frac{2b\cos\phi_0}{\cos^2\phi_0 - (a^2 - b^2)}, \tag{5.11}$$

$$\tan\delta_p = \frac{2\cos\phi_0\{2nka - (n^2 - k^2)b\}}{(a^2 + b^2) - (n^2 + k^2)^2 \cos^2\phi_0}, \tag{5.12}$$

and

$$\delta = \delta_p - \delta_s = \arctan\left[\frac{-2b\sin\phi_0\tan\phi_0}{(a^2 + b^2) - \sin^2\phi_0\tan^2\phi_0}\right]. \tag{5.13}$$

5.2 PCSA Configuration

Figure 5.1 defines the general experimental system and the coordinate system for a generic PCSA ellipsometer configuration. As the figure illustrates, PCSA denotes the order of optical elements encountered by light: polarizer (P), compensator (C), sample (S), and analyzer (A). We use right-hand coordinate system to specify the rotation angles of P, C, and A. The Y-axis is defined as perpendicular to the incident plane, whereas the X-axis is in the incident plane. The angle of the compensator is defined by the orientation of fast axis of compensator. The angles of polarizer and analyzer, which are both linear polarizers, are defined by their pass direction. All angles are positive in a counterclockwise sense, when viewed against the propagation direction of the beam. The polarization of the beam incident on the sample is controlled by the angles of P and C. The light reflected by the sample is analyzed by A. The detector then measures the intensity of the transmitted light.

Several types of ellipsometry can be performed with this collection of optical elements. We briefly review several. In null ellipsometry, a QWP is used as a compensator. In this

case either PCSA or PSCA configuration can be used. Null ellipsometry was operated manually in the past. In this mode, the compensator is held fixed at certain angles. The polarizer and analyzer are then rotated until the beam is extinguished. $\triangle$ and ψ are calculated using the setting of these polarizing optics and ultimately the refractive index of the material is obtained. Due to the manual nature of this technique, operation of null ellipsometry is very slow. Another disadvantage of a null ellipsometer is you have to use different compensators for different wavelengths. In principle, one could use null ellipsometry as the time-resolved null ellipsometry technique at a fixed time delay between the pump and the probe beam. This technique has been used to find the refractive index of Ge [74] and Si [75]. In these cases, null is not sensitive to the very small changes in the refractive index, so we cannot use this technique.

The next generation of ellipsometers came with rotating elements in the systems to overcome the disadvantages of a null ellipsometer. There are two type of common systems in this category: rotating polarizer (RPE) and rotating analyzer ellipsometry (RAE). These two types of configurations are performed without a compensator in the optical path, and it is easier to use it for different wavelengths. In each system, the signal is usually measured as a function of time, and is then Fourier analyzed in order to obtain the ellipsometric parameters Δ and ψ. A rotating analyzer ellipsometer is not accurate when measuring the imaginary part of refractive index when it is close to zero, and it also requires a polarization insensitive detector, and a highly depolarized source.

The third type of ellipsometer is a rotating compensator ellipsometer [76]. It has the advantage over the other two ellipsometers because it neither requires a polarization insensitive detector nor a highly depolarized source, since the polarizer and analyzer are fixed.

We have assembled a rotating compensator ellipsometer (PCSA). In this technique, one typically measures the time-resolved reflectivity of the sample at two different compensator angles at a given time delay between pump and probe. From these two sets of data, $\triangle n$

and $\triangle k$ are then calculated. Previously Choo *et al.* used this technique to study the carrier

dynamics in GeSi alloys [77].

5.3 Compensator: QWP or HWP?

In the PCSA configuration, one typically uses either a QWP or HWP as the compensator

C. The main factor involved in the choice is the sensitivity to changes in k.

In order to investigate the sensitivity to differences in k, we have calculated the reflec-

tivity as a function of compensator angle, ϕ_C, for fixed polarizer and analyzer angles, ϕ_P,

and ϕ_A. The calculation was done using the following equations [78]. For a quarter wave

plate, the reflectivity can be expressed as

$$
\begin{aligned}
R = \quad &\{\left(J^2 + K^2\right) R_p + \left(L^2 + M^2\right) R_s + 2\left(JL - KM\right) \sqrt{R_p R_s} \cos \delta \\
&+ 2(JM + KL) \sqrt{R_p R_s} \sin \delta\},
\end{aligned}
\tag{5.14}
$$

where

$$
J = \cos \Phi_A \cos \Phi_C \cos(\Phi_A - \Phi_C),
\tag{5.15}
$$

$$
K = \cos \Phi_A \sin \Phi_C \sin(\Phi_C - \Phi_P),
\tag{5.16}
$$

$$
L = \sin \Phi_A \sin \Phi_C \cos(\Phi_C - \Phi_P),
\tag{5.17}
$$

and

$$
M = \sin \Phi_A \cos \Phi_C \sin(\Phi_C - \Phi_P).
\tag{5.18}
$$

Here R_p, R_s, and $\delta = \delta_p - \delta_s$ are given by Eqs. 3.4, 3.5, 3.6, and 3.7. For an HWP as the

compensator, the reflectivity is given as

$$R = \{(J - K)^2 R_p + (L + M)^2 R_s + 2(J - K)(L + M)\sqrt{R_p R_s}\cos\delta\}. \qquad (5.19)$$

A typical result comparing sensitivity to k is shown in Fig. 5.2. Here we set $\phi_P = 0^0$, and $\phi_A = 45^0$ with an angle of incidence (or the sample) of 45^0. As the figure shows, a QWP provides slightly greater sensitivity to changes in k. We have, thus, chosen a QWP for our ellipsometer.
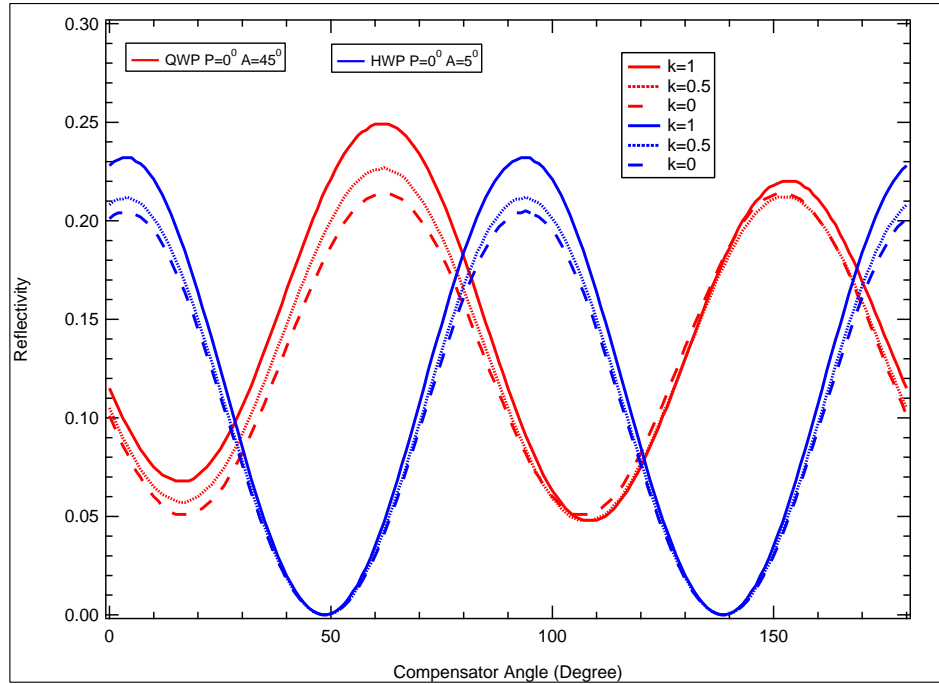
FIG. 5.2. Sensitivity comparison of quarter wave plate and half wave plate at an incident angle of 45 degrees.

5.4 Choice of Angles

We now describe how TRE can be used to determine changes in both n and k. As discussed in Chapter 3, the key quantities are the differential coefficients $\frac{1}{R}\frac{\partial R}{\partial n}$ and $\frac{1}{R}\frac{\partial R}{\partial k}$. Figure 5.3 plots the reflectivity, as well as these differential coefficients, as a function of

the compensator angle ϕ_C for $n = 3.66$, $k = 0.08$ (appropriate for GaAs), an incident angle of 45^0, $\phi_P = 10^0$, and $\phi_A = 10^0$, 30^0, 60^0, and 90^0. We first point out the differential coefficients for $\phi_A = 90^0$, which are insensitive to ϕ_C, are equivalent to the coefficient for straight s-polarized reflectivity (as expected since $\phi_A = 90^0$ results in detection of only the s component). As the figure clearly shows, $\phi_A = 90^0$ results in very low sensitivity to $\triangle k$. Conversely, other settings can result in comparable differential coefficients for n and k. For example, for $\phi_A = 30^0$, the two compensator angles $\phi_C = 35^0$ and $\phi_C = 125^0$, result in reasonably large values for $\frac{1}{R}\frac{\partial R}{\partial k}$, as well as $\frac{1}{R}\frac{\partial R}{\partial n}$. By making measurement at these two settings one could reasonably expect to distinguish the contributions of $\triangle n$ and $\triangle k$ to $\frac{\triangle R}{R}$, which is experimentally measured.

5.5   Experimental Setup

As illustrated in Fig. 5.4 we have assembled a PCSA ellipsometer for ultrafast ellipsometry. The probe pulse now passes through a linear polarizer (P) and a QWP compensator (C) before reflecting from the sample (S), passing through linear polarizer analyzer (A) and then being detected. In addition to the P, C, and A elements, several other elements have been added to maximize the efficiency of the ellipsometer. After the delay stage, the pump beam passes through a polarizer and half wave plate (Meadowlark AHM 050-840) before the sample. This polarizer is used to clean up the p-polarization. The HWP then rotates the pump polarization to minimize scattered pump light at the detector. As for the probe beam, it first encounters a beam splitter that is used to send one part of the probe beam to a reference Si photodetector. The main part of the probe beam then passes through a half wave plate in front of polarizer (P) in order to maximize the intensity through the polarizer.

5.6   Ellipsometer Alignment

Here we discuss the optical alignment of the four elements of the PCSA ellipsometer. Precise alignment is necessary in order to accurately extract $\triangle n$ and $\triangle k$ from the reflectiv-
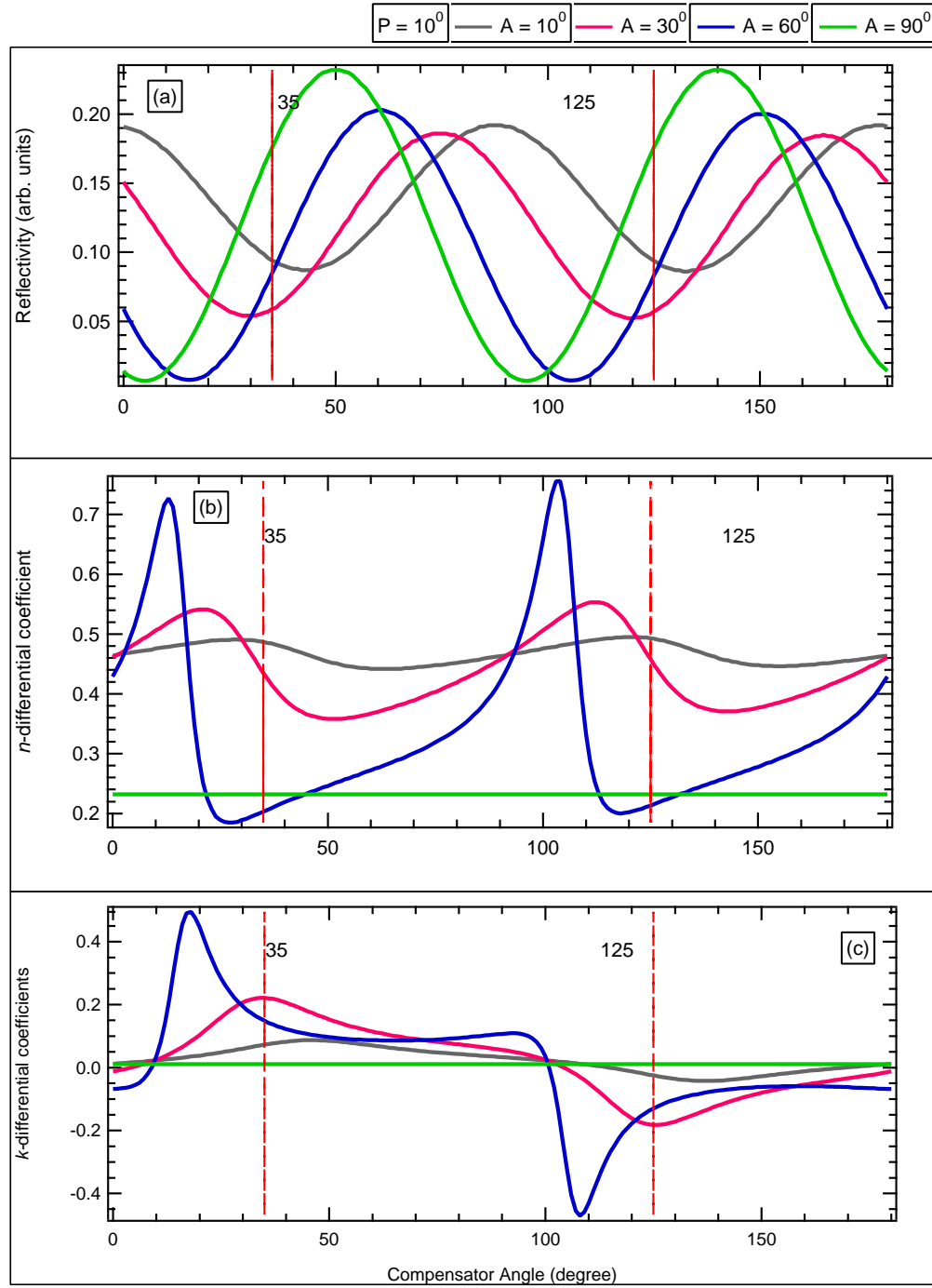
66

FIG. 5.3. *n* and *k* differential coefficients and GaAs reflectivity as a function of compensator angle (C) at three different angles of analyzer (A), at incident angle of 45^0, and polarizer angle at 10^0.
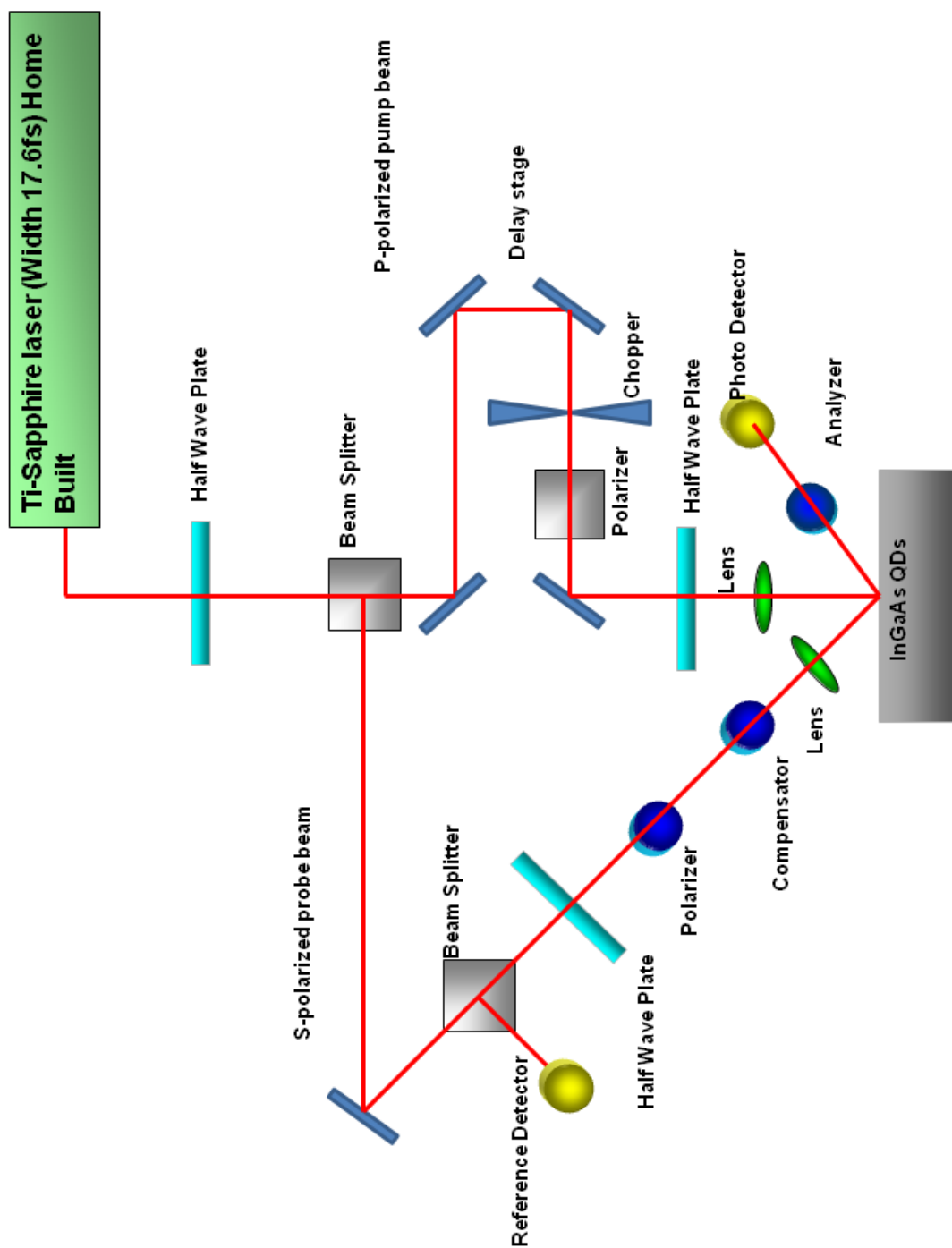
67

FIG. 5.4. Schematic of optical layout of PCSA ellipsometer used to measure time resolved ellipsometry (TRE).

ity measurements.

Both P and A elements are linear polarizers. Alignment is verified by obtaining the minimum transmission when $\phi_A = \phi_P \pm 90^0$. After the alignment of polarizers, we find the fast and slow axis of the QWP compensator. First, we place the QWP in between the crossed polarizers to determine the crystal axis. If there is no leakage or null is achieved in overall transmission, then the crystal axis is aligned parallel to polarizers. After the crystal axis is found, we identify the slow and fast axis of QWP. The fast and slow axes can be found be measuring the reflectivity of the sample, whose refractive index is known. For example, we set the polarizer and analyzer at 0^0 and 45^0, respectively, and change the compensator angle to determine the location of maximum transmission.

The sample has to be correctly aligned with respect to the axes of the polarizing optics. The sample surface must be in the plane where the linearly polarized beam is obtained by setting the P=0^0 and C=0^0 becomes a true *p*-polarized pulse to the sample. This can be achieved as follows, set both compensator and polarizer at 0^0 and ensure the laser beam is parallel to the optics table. Insert the sample and analyzer in the laser beam, and set the analyzer to 90^0. If the output of the analyzer is zero, that means the sample has been correctly installed. Repeat this procedure until null output is achieved.

5.7 Experimental verification

To verify the setup of our femtosecond ellipsometer, we perform a static reflectivity measurement on GaAs as function of compensator angle when $\Phi_P = 0^0$ and $\Phi_A = 0^0$. Figure 5.5 illustrates the theoretical and measured reflectivity response. Note the experimental results matches very closely to theoretical calculations. In our calculation, we vary the incident angle and refractive index as $\phi = 47.5^0$, $n = 3.76$, and $k = 0.08$ are obtained. The reported values of $n = 3.66$ and $k = 0.08$ at 800 nm are slightly different from what we got in our calculations Aspnes and Studna [79].
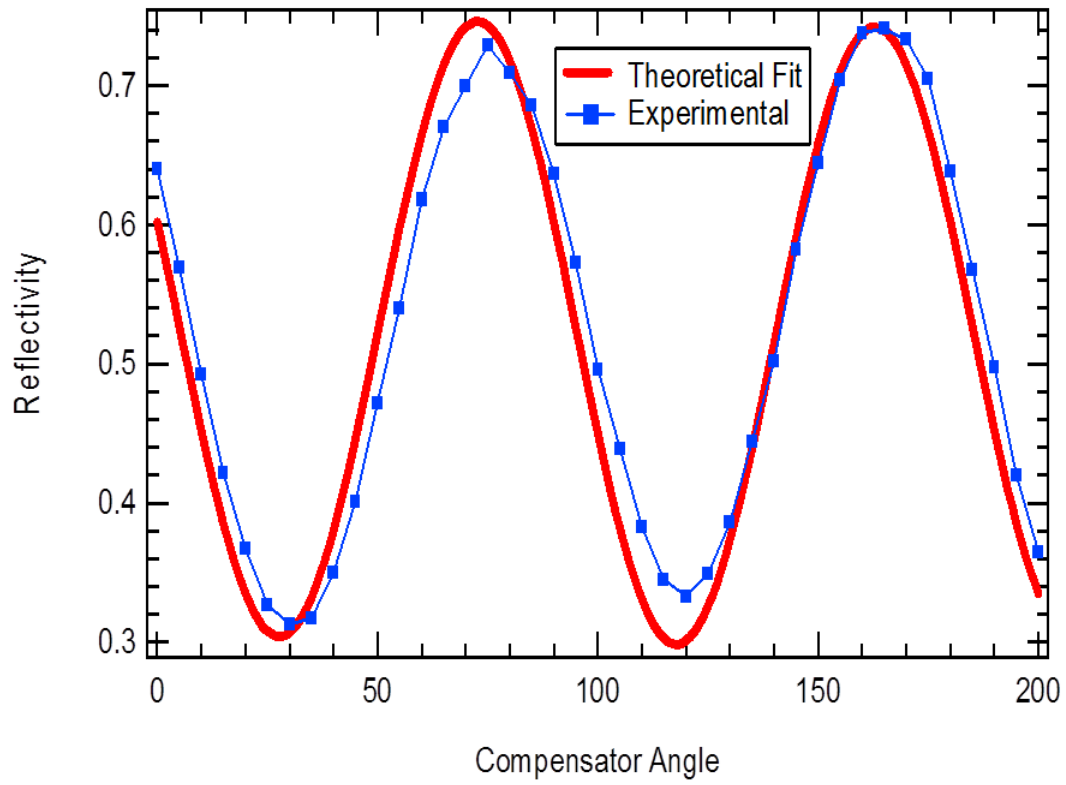
FIG. 5.5. Reflectivity of GaAs vs. compensator angle at polarizer angle $\Phi_P = 0^0$ and analyzer angle $\Phi_A = 45^0$.

CHAPTER 6

CONCLUSION

6.1   Summary

In our lab, we have a home-built Ti-sapphire laser with 28 fs laser pulse at 800 nm. Using the time-resolved reflectivity experiment, we have done three total time delay scans on our InGaAs/GaAs quantum dot samples: 5 ps, 25 ps, and 120 ps. Also, we have measured the reflectivity at seven different neutral density filters where laser intensity increases from 2.4% to 100%.

We have investigated the carrier dynamics of InGaAs QDs. Using Eq. 4.1 to find four different relaxation time constants. The relaxation times τ_1, τ_2, and τ_3 are extracted from our least-square fitting analysis, where as τ_1 is the momentum and /or energy relaxation rate [15, 16, 18], τ_2 is the capture time of carriers by the InGaAs layer, and τ_3 is the carrier relaxation rate within the layer. The term with $\tau_4 = \infty$ is used to describe the nonzero offset that is still present at the end of the 120 ps scan.

Our results of least-square fitting analysis of thick-capped layer InGaAs samples A, B, D, and E gives the value of capture time; τ_2 is between 1 and 2 ps for all laser intensities. The relaxation time, τ_3, of samples as a function of laser intensity is as follows. For sample B, τ_3 varies from ~ 40 ps to ~ 100 ps as the laser intensity is increased. For sample D, this relaxation time varies from ~ 4 ps to ~ 14 ps as the laser intensity is increased. For sample A, τ_3 varies from ~ 50 ps at lowest intensity to ~ 30 ps at highest intensity. For sample A τ_3 varies from ~ 4 ps to ~ 14 ps as the laser intensity is increased. Lastly, for sample E, the longest relaxation time, τ_3, decreases from ~ 300 ps to ~ 17 ps as the laser intensity is increased. There is no consistent trend in τ_3 versus laser intensity among the thick-capped quantum dots samples.

For thin-capped InGaAs QD samples, our reflectivity analysis uses three different relaxation time constants to find the carrier capture time and relaxation time. The times τ_2

and τ_3 are extracted form the analysis where as τ_2 is the capture time of carriers by the InGaAs layer, and τ_3 is the carrier relaxation rate within the layer. Again, the term with $\tau_4 = \infty$ is used to describe the nonzero offset that is still present at the end of the 120 ps scan.

The capture time, τ_2, of thin-cap QD samples versus a laser intensity tends to increase. For sample I, τ_2 increases from ~0.46 ps to ~7.8 ps. For sample G, capture time, τ_2, increases from ~ 0.21 ps at lower laser intensities to ~ 0.51 ps at the highest intensity. For sample F, capture time, τ_2, varies from ~ 0.29 ps to ~ 0.6 ps as the laser intensity is increased. The general trend of τ_2 increasing with laser intensity can be attributed to the state filling.

The longest relaxation time τ_3 of the thin-cap InGaAs QD sample I τ_3 varies from ~ 440 ps to ~ 180 ps as the laser intensity is increased. For sample G, τ_3 varies from ~ 15 ps to ~ 3 ps as the laser intensity is increased. For sample F, τ_3 decreases from ~ 59 ps at the minimum intensity to ~ 16 ps at the highest intensity. The general trend of τ_3 decreasing with increasing laser intensity suggests carrier-carrier scattering is key to relaxation within the InGaAs layer.

We have studied the carrier dynamics of thin and thick InGaAs QD using ultrafast pump-probe reflectivity. From our measurements we have deduced capture times depend on the annealing temperature, cap thickness, and the size of the quantum dots. In principle, we excite the carrier in GaAs with the laser intensity of 1.55 eV. Electron hole pairs are created in the barrier of GaAs where GaAs is either 100 nm or 10 nm. After the electron hole pairs are created, they subsequently get captured to QD energy levels. The capture time for 100-nm cap thickness QDs is slower than the 10-nm of GaAs thin samples. This suggests that transport of carriers plays an important role in the carrier dynamics of QDs.

We have also found capture time decreases as the annealing temperature for thin-capped quantum dot samples increases. The data suggest slower capture times for the lower an-

nealing temperature as QDs. Those are formed at higher annealing temperature have wider

bases and smaller heights, indicating that QD morphology affects carrier capture.

6.2 Future work

We have designed the femtosecond-time-resolved ellipsometer using the PCSA configuration to study carrier dynamics in InGaAs/GaAs quantum dots. It is a powerful technique that gives the information about the complex refractive index. In this experiment, we can determine both real and imaginary parts of refractive index. We can measure the two different sets of differential reflectivity $\left[\frac{\triangle R}{R}(t)\right]$ at two different compensator angles but constant polarizer and analyzer angles. Using this experimentally observed reflectivity, we can use Eq. 3.8 to find out the real part and the imaginary part of refractive index. Carrier dynamics investigated via pump-probe reflectivity typically provides information on the change in the real part of the refractive index. But, in order to directly access the change in absorption, we need to probe changes in the imaginary part of the refractive index. Thus, time-resolved ellipsometric measurements can give full information about the refractive index of the semiconductor quantum dots and will thus give more insight into carrier dynamics, as compared to simple pump and probe reflectivity.

REFERENCES

[1] N. N. Ledenstov, *Proceeding of the 23rd International Confernce on Physics of Semi-conductors* (World Scientific, Singapore, 1996).

[2] L. Esaki and R. Tsu, IBM Research Note , 61 (1970).

[3] L. Esaki and R. Tsu, IBM J. Res. Develop. , RC 2418 (1969).

[4] R. Dingle, W. Wiegmann, and C. H. Henry, Phys. Rev. Lett. **33**, 827 (1974).

[5] L. L. Chang, L. Esaki, and R. Tsu, Appl. Phys. Lett. **24**, 593 (1974).

[6] P. M. Petroff, A. C. Gossard, R. A. Logan, and W. Wiegmann, Appl. Phys. Lett. **41**, 635 (1982).

[7] M. A. Reed, R. T. Bate, K. Bradshaw, W. M. Duncan, W. R. Frensley, J. W. Lee, and H. D. Shih, J. Vac. Sci. Tech.: Microelectronics and Nanometer Structures **4**, 358 (1986).

[8] I. N. Stranski and L. Krastanow, Akademie der Wissenschaften Wien **146**, 797 (1938).

[9] G. Sek, P. Poloczek, K. Ryczko, J. Misiewicz, A. Löffler, J. P. Reithmaier, and A. Forchel, J. Appl. Phys. **100**, 103529 (2006).

[10] P. Petroff and S. DenBaars, Superlattices and Microstructures **15**, 15 (1994).

[11] P. B. Joyce, T. J. Krzyzewski, G. R. Bell, B. A. Joyce, and T. S. Jones, Phys. Rev. B **58**, R15981 (1998).

[12] D. J. Kim, E. A. Everett, and H. Yang, J. Appl. Phys. **101**, 106106 (2007).

[13] J. Abel, D. J. Kim, E. A. Everett, and H. Yang, J. Cryst. Growth **310**, 2244 (2008).

[14] J. Shah, *Hot Carries in Semiconductor Nanostructures* (Springer-Verlag, Berlin, 1992).

[15] W. A. Hügel, M. F. Heinrich, M. Wegener, Q. T. Vu, L. Bányai, and H. Haug, Phys. Rev. Lett. **83**, 3313 (1999).

[16] P. C. Becker, H. L. Fragnito, C. H. B. Cruz, R. L. Fork, J. E. Cunningham, J. E. Henry, and C. V. Shank, Phys. Rev. Lett. **61**, 1647 (1988).

[17] J. L. Oudar, A. Migus, D. Hulin, G. Grillon, J. Etchepare, and A. Antonetti, Phys. Rev. Lett. **53**, 384 (1984).

[18] M. T. Portella, J.-Y. Bigot, R. W. Schoenlein, J. E. Cunningham, and C. V. Shank, Appl. Phys. Lett. **60**, 2123 (1992).

[19] J. Nunnenkamp, J. H. Collet, J. Klebniczki, J. Kuhl, and K. Ploog, Phys. Rev. B **43**, 14047 (1991).

[20] J. H. Collet, S. Hunsche, H. Heesel, and H. Kurz, Phys. Rev. B **50**, 10649 (1994).

[21] S. Bar-Ad, P. Kner, M. V. Marquezini, D. S. Chemla, and K. El Sayed, Phys. Rev. Lett. **77**, 3177 (1996).

[22] F. X. Camescasse, A. Alexandrou, D. Hulin, L. Bányai, D. B. Tran Thoai, and H. Haug, Phys. Rev. Lett. **77**, 5429 (1996).

[23] A. Alexandrou, V. Berger, and D. Hulin, Phys. Rev. B **52**, 4654 (1995).

[24] P. Langot, N. Del Fatti, D. Christofilos, R. Tommasi, and F. Vallée, Phys. Rev. B **54**, 14487 (1996).

[25] J. Siegert, S. Marcinkevičius, and Q. X. Zhao, Phys. Rev. B **72**, 085316 (2005).

[26] S. Marcinkevičius and R. Leon, Phys. Rev. B **59**, 4630 (1999).

[27] K. W. Sun, J. W. Chen, B. C. Lee, C. P. Lee, and A. M. Kechiantz, Nanotechnology **16**, 1530 (2005).

[28] A. V. Uskov, J. McInerney, F. Adler, H. Schweizer, and M. H. Pilkuhn, Appl. Phys. Lett. **72**, 58 (1998).

[29] R. Ferreira and G. Bastard, App. Phys. Lett. **74**, 2818 (1999).

[30] J.-Z. Zhang and I. Galbraith, Appl. Phys. Lett. **89**, 153119 (2006).

[31] S. B. B. T. I. Magnusdottir, A. V. Uskov and J. Mork, J. Appl. Phys. **92**, 5982 (2002).

[32] T. S. Sosnowski, T. B. Norris, H. Jiang, J. Singh, K. Kamath, and P. Bhattacharya, Phys. Rev. B **57**, R9423 (1998).

[33] H.-Y. Liu, Z.-M. Meng, Q.-F. Dai, L.-J. Wu, Q. Guo, W. Hu, S.-H. Liu, S. Lan, and

T. Yang, J. Appl. Phys. **103**, 083121 (2008).

[34] Q. Li, Z. Xu, and W. Ge, Solid State Commun. **115**, 105 (2000).

[35] T. Müller, F. F. Schrey, G. Strasser, and K. Unterrainer, Appl. Phys. Lett. **83**, 3572 (2003).

[36] J. Urayama, T. B. Norris, H. Jiang, J. Singh, and P. Bhattacharya, Appl. Phys. Lett. **80**, 2162 (2002).

[37] L. Zhang, T. F. Boggess, K. Gundogdu, M. E. Flatté, D. G. Deppe, C. Cao, and O. B. Shchekin, Appl. Phys. Lett. **79**, 3320 (2001).

[38] C. Lobo, R. Leon, S. Marcinkevicius, W. Yang, P. C. Sercel, X. Z. Liao, J. Zou, and D. J. H. Cockayne, Phys. Rev. B **60**, 16647 (1999).

[39] S. Marcinkevicius and R. Leon, Appl. Phys. Lett. **76**, 2406 (2000).

[40] T. R. Nielsen, P. Gartner, and F. Jahnke, Phys. Rev. B **69**, 235314 (2004).

[41] A. V. Uskov, F. Adler, H. Schweizer, and M. H. Pilkuhn, J. Appl. Phys. **81**, 7895 (1997).

[42] X.-Q. Li, H. Nakayama, and Y. Arakawa, Phys. Rev. B **59**, 5069 (1999).

[43] D. F. Schroeter, D. J. Griffiths, and P. C. Sercel, Phys. Rev. B **54**, 1486 (1996).

[44] Y. Toda, O. Moriwaki, M. Nishioka, and Y. Arakawa, Phys. Rev. Lett. **82**, 4114 (1999).

[45] A. Vasanelli, R. Ferreira, and G. Bastard, Phys. Rev. Lett. **89**, 216804 (2002).

[46] E. W. Bogaart, R. Notzel, Q. Gong, J. E. M. Haverkort, and J. H. Wolter, Appl. Phys. Lett. **86**, 173109 (2005).

[47] J. Urayama, T. B. Norris, J. Singh, and P. Bhattacharya, Phys. Rev. Lett. **86**, 4930 (2001).

[48] R. Heitz, H. Born, F. Guffarth, O. Stier, A. Schliwa, A. Hoffmann, and D. Bimberg, Phys. Rev. B **64**, 241305 (2001).

[49] K. Ikeda, H. Sekiguchi, F. Minami, J. Yoshino, Y. Mitsumori, H. Amanai, S. Nagao,

and S. Sakaki, J. Lumin. **108**, 273 (2004).

[50] K. Gündogdu, K. C. Hall, T. F. Boggess, D. G. Deppe, and O. B. Shchekin, Appl. Phys. Lett. **85**, 4570 (2004).

[51] S. Marcinkevicius, A. Gaarder, and R. Leon, Phys. Rev. B **64**, 115307 (2001).

[52] M. Wesseli, C. Ruppert, S. Trumm, H. J. Krenner, J. J. Finley, and M. Betz, Phys. Status Solidi B **243**, 2217 (2006).

[53] A. J. Sabbah and D. M. Riffe, Phys. Rev. B **66**, 165217 (2002).

[54] R. M. Azzam and N. M. Bashara, *Ellipsometry and Polarized Light* (North-Holland Publ., Amsterdam, 1977).

[55] M. T. Asaki, C.-P. Huang, D. Garvey, J. Zhou, H. C. Kapteyn, and M. M. Murnane, Opt. Lett. **18**, 977 (1993).

[56] D. M. Riffe and A. J. Sabbah, Rev. Sci. Instrum. **69**, 3099 (1998).

[57] M. Born and E. Wolf, *Principle of Optics* (Pergamon Press, New York, 1983).

[58] U. Bockelmann and T. Egeler, Phys. Rev. B **46**, 15574 (1992).

[59] R. Heitz, M. Grundmann, N. N. Ledentsov, L. Eckey, M. Veit, D. Bimberg, V. M. Ustinov, A. Y. Egorov, A. E. Zhukov, P. S. Kop'ev, and Z. I. Alferov, Appl. Phys. Lett. **68**, 361 (1996).

[60] R. D. Schaller, J. M. Pietryga, S. V. Goupalov, M. A. Petruska, S. A. Ivanov, and V. I. Klimov, Phys. Rev. Lett. **95**, 196401 (2005).

[61] L. Zhang, T. F. Boggess, D. G. Deppe, D. L. Huffaker, O. B. Shchekin, and C. Cao, Appl. Phys. Lett. **76**, 1222 (2000).

[62] G. Wang, S. Fafard, D. Leonard, J. E. Bowers, J. L. Merz, and P. M. Petroff, Appl. Phys. Lett. **64**, 2815 (1994).

[63] U. Bockelmann and G. Bastard, Phys. Rev. B **42**, 8947 (1990).

[64] F. Adler, M. Geiger, A. Bauknecht, F. Scholz, H. Schweizer, M. H. Pilkuhn, B. Ohnesorge, and A. Forchel, J. Appl. Phys. **80**, 4019 (1996).

[65] R. Heitz, M. Veit, N. N. Ledentsov, A. Hoffmann, D. Bimberg, V. M. Ustinov, P. S. Kop'ev, and Z. I. Alferov, Phys. Rev. B **56**, 10435 (1997).

[66] S. Raymond, S. Fafard, P. Poole, A. Wojs, P. Hawrylak, C. Gould, S. Sachrajda, S. Charbonneau, D. Leonard, R. Leon, P. Petroff, and J. Merz, Superlattices and Microstructures **21**, 541 (1997).

[67] S. Grosse, J. H. H. Sandmann, G. von Plessen, J. Feldmann, H. Lipsanen, M. Sopanen, J. Tulkki, and J. Ahopelto, Phys. Rev. B **55**, 4473 (1997).

[68] X. M. Wen, L. V. Dao, P. Hannaford, S. Mokkapati, H. H. Tan, and C. Jagadish, J. Physics: Condensed Matter **19**, 386213 (2007).

[69] P. Drude, Ann. Phys. Chem. **36**, 532 (1889).

[70] L. Tronstad, Trans. Faraday Soc. **29**, 502 (1933).

[71] A. Rothen, Rev. Sci. Instrum. **16**, 26 (1945).

[72] R. H. Muller, Surf. Sci. **16**, 14 (1969).

[73] J. A. Stratton, *Electromagnetic Theory* (McGraw-Hill, New York, 1941).

[74] D. H. Auston and C. V. Shank, Phys. Rev. Lett. **32**, 1120 (1974).

[75] J. G. E. Jellison and D. H. Lowndes, Appl. Phys. Lett. **47**, 718 (1985).

[76] P. Hauge and F. Dill, Opt. Commun. **14**, 431 (1975).

[77] H. R. Choo, X. F. Hu, M. C. Downer, and V. P. Kesan, Appl. Phys. Lett. **63**, 1507 (1993).

[78] H. R. Choo, Ph.D. dissertation, University of Texas, Austin (1993).

[79] D. E. Aspnes and A. A. Studna, Phys. Rev. B **27**, 985 (1983).

CURRICULUM VITAE

Kripa Nidhan Chauhan
(November 2012)

772 North 750 East, Apt 3   (435) 232-7456
Logan, UT 84321   chauhankripa@gmail.com

EXPERTISE

• Ultrafast Spectroscopy, Solid State and Surface Physics

• Femtosecond Laser Systems Ti-Sapphire

• Spectroscopic Studies and Interpretation

• Spectroscopic Ellipsometry

• Carrier Dynamics in Semiconductors

• Thin / Thick Film and Bulk Growth of Materials

• Usage and Implementation of High Vacuum and Cryogenics Techniques

WORK EXPERIENCE

Graduate Research Student Sept 2005-present

Utah State University Logan, Utah

• Design and construction of time-resolved femtosecond ellipsometry (TRE) technique for semiconductors to study the change in both real and absorptive part of dielectric function

• Characterization of LT-GaAs, GaAs and InGaAs/GaAs Quantum Dots

• Surface Passivation studies on LT-GaAs, GaAs

• Time-resolved differential reflectivity (TRDR) measurements on semiconductors to study the change in real part of dielectric function

• Spectroscopic Ellipsometry of InGaAs/ GaAs Quantum Dots

Graduate Teaching Assistant Sept 2004-present

Utah State University, Logan, Utah

• Instructor Phyx 2225, 2215 Physics for Scientist and Engineers Lab Course (Designed Lab Manuals)

• Teaching Physics Labs (20 Students) for Engineering and Premed

• Weekly Problem Solving Sessions for Physics Students

• Setup All of the Physics Labs for Engineering and Premed Students

Project Assistant July 2002-July 2004

Department of Physics & Astrophysics, University Of Delhi, Delhi, India

Kinetics of Defect Studies in High Temperature Superconductor (HTSC)

• Proficient in design and operation of DC Sputtering system

• Synthesis, analysis and characterization of bulk, thin film YBCO

• Design and construction of low temperature cryostat (77 Kelvin)

• Magneto-resistance techniques to study the effect of defects

EDUCATION

Ph.D. Physics (expected 12/12)	**Utah State University**, Logan, UT Dissertation: *Carrier dynamics in InGaAs/GaAs quantum dots excited by femtosecond pulses.* Major Professor: D. Mark Riffe
M.S. May 2002	**University of Delhi,** Delhi, India Physics (Specialization in Experimental Solid State Physics)
B.S. May 2000	**University of Delhi,** Delhi, India Physics (Honors), Ranked II

RESEARCH SKILLS

• Ti-sapphire oscillator Operation and maintenance

• Diode-pumped Nd:Vanadate, 5W @ 532nm

• Pump-probe reflectivity to study the carrier dynamics

• Spectroscopic Ellipsometry

• Femtosecond Ellipsometry

• Operation of high temperature furnaces

• Sputtering of Materials

• Hydraulic pressure dyes

• Low temperature measurements (77 Kelvin)

TECHNICAL SKILLS

• Operating Systems: Windows, OS X

• Applications: Word, Excel, Power Point

• Scientific Applications: Wvase32, IGOR Pro, MathCad, Lyx, Maple

• Programming Languages: Lab View, FORTRAN, C, Pascal

• Extensive knowledge of computer automation and device interfacing using GPIB, RS232, National Instruments and PCI computer boards

HONORS

• Howard L. Blood Scholarship Summer 2009

• Student Travel Grant, USU 2005, 2010

• UGC Project Fellowship, Department of Physics and Astrophysics, University of Delhi 2002-2004

• Ranked IInd in College, Bachelor of Science, Physics 1999, 2000

PUBLICATIONS AND PRESENTATIONS

2012 (under preparation)	**Carrier Capture dynamics of Single InGaAs/GaAs Quantum Dots Layers.** K. N. Chauhan, D.M. Riffe, E. A. Everett, D. J. Kim, H. Yang, and F. K. Shen
2010	**"Femtosecond pump-probe reflectivity study of InGaAs/GaAs quantum dots carrier dynamics"** *KN Chauhan, DM Riffe APS Four Corner Meeting, Ogden, Utah 2010*
2010	**Carrier Dynamics in InGaAs/GaAs Quantum Dots Excited by Degenerate Pump-Probe Technique** *KN Chauhan, DM Riffe Annual Meeting of the American Physical Society, Portland, March 2010*
2009	**Carrier Dynamics in InGaAs/GaAs Quantum Dots** *Colloquium, Department of Physics, Fall Utah State University 2009*
2008	**Semiconductor Solar Cells** *Surface Science Seminar, Spring USU 2008*
2005	**Semiconductor GaAs Dielectric Functions are Measured by Using Femtosecond Ellipsometry** *Surface Science Seminar, Spring Utah State University 2005*
2005	**Real Time Measurement of Semiconductor Dielectric Functions Using Femtosecond Ellipsometry** *KN Chauhan, DM Riffe APS Four Corner Meeting, Boulder, October 2005*